NASA Technical Paper 1385

Onset of Condensation Effects With an NACA 0012-64 Airfoil Tested in the Langley 0.3-Meter Transonic Cryogenic Tunnel

Robert M. Hall

APRIL 1979

NASA

NASA Technical Paper 1385

Onset of Condensation Effects With an NACA 0012-64 Airfoil Tested in the Langley 0.3-Meter Transonic Cryogenic Tunnel

Robert M. Hall
Langley Research Center
Hampton, Virginia

NASA
National Aeronautics
and Space Administration

Scientific and Technical
Information Office

1979

SUMMARY

A 0.137-meter NACA 0012-64 airfoil has been tested at a 0° angle of attack in the nitrogen-gas Langley 0.3-meter transonic cryogenic tunnel at free-stream Mach numbers of 0.75, 0.85, and 0.95 over a total pressure range from 1.2 to 5.0 atmospheres. The onset of condensation effects as determined by varying stagnation temperature was found to correlate better with the amount of supercooling in the free stream than it did with the supercooling in the region of maximum local Mach number over the airfoil. Effects in the pressure distribution over the airfoil were generally seen to appear over its entire length at nearly the same total temperature. Both observations suggest that heterogeneous nucleation does occur in the free stream. The present results are compared to calculations made by Sivier and data gathered by Goglia. The potential operational benefits realized from supercooling are presented in terms of increased Reynolds number capability at a given tunnel total pressure and reduced drive-fan power and liquid nitrogen consumption if Reynolds number is held constant. Depending on total pressure and free-stream Mach number, these three benefits are found to vary respectively from 8 to 19 percent, 12 to 24 percent, and 9 to 19 percent. An appendix is included which gives details of the data analysis and error estimates for the differences in pressure distributions.

INTRODUCTION

Cryogenic wind tunnels should normally be operated at the lowest possible total temperatures in order to maximize Reynolds number capability for a given total pressure and to minimize operating costs. The minimum operating temperatures are, however, limited by low-temperature behavior of the test gas. Either the test gas begins to condense or its equation of state changes so that the gas does not properly simulate the nearly ideal-gas behavior of air encountered in flight. By analyzing the equation of state for nitrogen gas over the operating ranges of existing and proposed transonic cryogenic wind tunnels, Adcock showed in reference 1 that low-temperature nitrogen approximates an ideal gas during flow simulations for total pressures under 10 atmospheres and for Mach numbers up to 2. Consequently, for operating conditions within these limits, the lower temperature boundary appears to be determined by the onset of condensation of the nitrogen test gas. The low-temperature boundary is important from an operational viewpoint because it determines, on the one hand, the maximum Reynolds number capability for a fixed tunnel total pressure and, on the other hand, the most economical total temperature and pressure at which to operate the tunnel for a fixed test Reynolds number.

The present condensation investigation employs a pressure-instrumented 0.137-meter NACA 0012-64 airfoil mounted at 0° angle of attack in the Langley 0.3-meter transonic cryogenic tunnel. Changes in the pressure distribution over the airfoil were used to detect the onset of condensation effects at transonic speeds just as changes in pressure distributions in divergent nozzles were used in references 2 to 6 to detect the onset of condensation effects at supersonic

and hypersonic speeds. The airfoil was tested at free-stream Mach numbers of 0.75, 0.85, and 0.95 over a total pressure range of 1.2 to 5.0 atmospheres in order to determine for a range of Mach numbers and pressures the total temperature at which condensation influences the flow about the airfoil.

A goal of the Langley condensation program is predicting the onset of condensation effects not only in the 0.3-meter tunnel but in larger tunnels such as the National Transonic Facility (2.5-meter square test section) under construction at the Langley Research Center. At the present time, however, how to extend the results presented herein to a larger facility is not clear. The larger tunnel circuit should allow more time for the evaporation of the injected liquid nitrogen used for absorbing the heat of the drive fan. As discussed later in this paper, this added time could decrease the severity of heterogeneous nucleation. But, with longer test sections and wing chord lengths, the larger tunnels will be much more susceptible to increased droplet growth both in the test section and over the model. The question of the effects of length needs to be addressed before the present results can be confidently extended to other facilities.

SYMBOLS

a	speed of sound, m/sec
C_p	static pressure coefficient, $\frac{p - p_\infty}{q_\infty}$
ΔC_p	difference in C_p defined by equation (A6)
c	airfoil chord, 0.137 m
i	summation index
M	Mach number
m	slope of linear regression fit defined by equation (A1)
n	number of condensation-free pressure distributions along a path of nominally constant Mach and Reynolds numbers
p	pressure, atm (1 atm = 101 kPa)
q	dynamic pressure, atm
R	Reynolds number per meter
R_c	chord Reynolds number per meter
r	correlation coefficient as defined in equation (A4)
T	temperature, K

ΔT supercooling defined by equation (1), K

x linear dimension along airfoil chord line, m

μ viscosity, $N\text{-}s/m^2$

ρ density, kg/m^3

σ standard deviation

Subscripts:

e conditions along the isentrope at onset of condensation effects

l local conditions

o values corrected for Mach number effect

s conditions at intersection of isentrope and vapor pressure curve

t total conditions

∞ free-stream conditions

Abbreviations:

LN_2 liquid nitrogen

min. minimum

sat. saturation

A bar over a symbol indicates a mean value.

MINIMUM OPERATING TEMPERATURES

The minimum operating temperature, as determined by the onset of condensation, has an impact on both the maximum Reynolds number capability and the operating cost of nitrogen-gas cryogenic wind tunnel cooled by injection of liquid nitrogen. The reasons for these effects can be understood by reviewing the effects of changing tunnel temperature upon the test gas. As shown in figure 1(a), the density ρ increases while the viscosity μ and the speed of sound a decrease as the total temperature T_t decreases for a fixed value of tunnel total pressure p_t. As shown in figure 1(b), this behavior of the gas properties as T_t decreases leads to a dramatic increase in unit Reynolds number R, a decrease in drive power required, and no change in dynamic pressure q. Since the rate of increase in R is itself increasing at the lower temperatures, it is important to operate the tunnel at as low a temperature as possible. The low-temperature limit obviously fixes the maximum R capability of a cryogenic tunnel running at its highest possible pressure. However, if this maximum R capability is not necessary, the minimum temperature boundary

impacts on the operating costs of the tunnel. The greater the gain in R due to low-temperature operation, the less p_t is required to obtain the operating R of interest. Since drive-fan power is proportional to p_t and decreases with decreasing T_t, minimizing T_t reduces drive-fan power and, consequently, reduces the amount of injected liquid nitrogen required to absorb the heat of the drive fan. Both reductions decrease direct operating costs, which are split with about 90 percent going to the injected liquid nitrogen and only 10 percent going to power the drive fan. (Specific details about drive power required and operating costs are given in refs. 7 and 8.)

To estimate the minimum operating temperature for a given value of tunnel total pressure, one might choose the value of tunnel total temperature which would just allow saturation to occur at the maximum local Mach number $M_{l,max}$ over the test model. However, references 2 to 6 as well as investigators working in the Langley 0.3-meter transonic cryogenic tunnel point out that the onset of condensation effects tends to occur below saturation temperatures. The amount of this temperature difference is normally measured by the supercooling at the onset of condensation effects ΔT which is defined as

$$\Delta T = T_s - T_e \tag{1}$$

where T_s is the static temperature at the point where the isentrope crosses the vapor pressure curve and T_e is the static temperature on the isentrope where effects are first seen. The magnitude of the supercooling for various tunnel pressures and Mach numbers determines the minimum operating temperatures and, consequently, the maximum benefits to be gained from cryogenic operation.

EXPERIMENTAL APPARATUS

Tunnel

The Langley 0.3-meter transonic cryogenic tunnel is a continuous flow, fan-driven tunnel, which uses nitrogen as a test gas and is cooled by injecting liquid nitrogen directly into the stream. Variation of the rate of liquid nitrogen injection provides an approximate total temperature range from 80 to 350 K, while the total pressure can be varied from 1.2 to 5.0 atm. The combined low temperature and high pressure can produce a Reynolds number of over 330×10^6 per meter. Some of the design features and operational characteristics of the 0.3-meter tunnel have been reported by Kilgore in reference 9. A sketch of the 0.3-meter tunnel is shown in figure 2.

The liquid nitrogen used to cool the tunnel and absorb the heat of the drive fan is injected into the tunnel through a series of 11 nozzles arranged on three different struts, or spray bars, at the three injection stations shown in figure 2. Full details of this arrangement are included in reference 9. However, for one of the tests during the present investigation (details to be mentioned in the section entitled "Results and Discussion"), the spray-bar system was removed and injection was carried out by injection through just four

nozzles at injection station 1. This change, of course, necessitated larger liquid-flow rates per nozzle.

Airfoil and Installation

A 0.137-m NACA 0012-64 airfoil was used for these tests. The airfoil had 20 pressure orifices spaced at 5 percent chord intervals on both the top and bottom surfaces with the first orifice at the leading edge. For the tests at M_∞ values of 0.75 and 0.95, a rearward-facing orifice was added to the trailing edge of the airfoil. The airfoil was installed between flats in the octagonal test section, with the leading edge 0.62 m from the beginning of the test section. The angle of attack of the airfoil was zero for all tests. A sketch of the airfoil is given in figure 3.

The pressure distributions over the airfoil may be influenced by wall interference effects because of the relatively large chord of the airfoil compared to the size of the test section. However, wall interference should not affect the occurrence of condensation, and no attempt has been made to correct the data for wall interference effects.

Data Acquisition and Error Estimate

The tunnel parameters were first recorded; then a differential pressure transducer was used in a scanning-valve system to step through and record the pressures around the airfoil. The time to acquire all of the data for a complete pressure distribution was 50 sec. During the 50-sec acquisition period, the tunnel conditions were observed to fluctuate by the following amounts: M_∞, ± 0.003; T_t, ± 0.5 K; and p_t, ± 0.002 to ± 0.012 atm, depending on p_t itself.

The manufacturer specified the accuracy of the pressure transducer to be 0.5 percent of full scale. However, the precision of the transducer proved to be an order of magnitude better than the specified accuracy based upon scatter in the values of pressure from data point to data point and from day to day. For the transducer used in the tests at $M_\infty = 0.75$ and 0.95, the precision was ± 0.0004 atm. For the smaller transducer used in the test at $M_\infty = 0.85$, the precision was ± 0.0002 atm. There was no significant error introduced by either the signal-conditioning or data-acquisition systems. An estimate of the uncertainty in C_p due to the imprecision of the pressure transducers and the fluctuating tunnel conditions is given in the appendix.

TESTS

Data Sampled

To determine the total temperature at which condensation effects do occur and to investigate the influence of free-stream Mach number and total pressure on the onset of condensation effects, the airfoil was tested at free-stream Mach numbers of 0.75, 0.85, and 0.95 over a total pressure range of 1.2 to

5.0 atm. The test envelopes were bounded in p_t by the 1.2- to 5.0-atm pressure limits of the tunnel and were bounded in T_t by total temperatures corresponding to saturated flow at $M_{l,max}$ and those corresponding to saturation in the reservoir section. Total conditions which fall lower in T_t than the reservoir saturation line are unobtainable since the injected liquid nitrogen used for cooling cannot provide cooling when T_t is below the vapor-pressure curve. Total temperatures above those along the line of local saturation offer no possibility of condensation in a pure nitrogen test gas so they are used in this study only as a way of obtaining data unaffected by condensation effects for comparison purposes.

To explore each of the regions of interest in the p_t and T_t plane, paths of constant chord Reynolds number R_c and M_∞ were used to traverse the region of interest. Since along each of the paths both M_∞ and R_c were held constant, systematic deviation in pressure coefficients at any x/c position over the airfoil was taken to be the result of condensation effects. Five paths of constant R_c and M_∞ are shown for the $M_\infty = 0.85$ test in figure 4. The R_c along each path varied from 16×10^6 at the low-pressure traverse to 42×10^6 at the high-pressure traverse. Along these five paths, a total of 201 pressure distributions were recorded and analyzed. Similar envelopes were drawn and investigated for $M_\infty = 0.75$ and $M_\infty = 0.95$, except that only three paths of constant R_c and M_∞ were used in these cases. These envelopes are shown in figures 5 and 6. During the investigation of the high-pressure path for the $M_\infty = 0.95$ test, a fan drive-power limit was encountered so M_∞ was reduced from 0.95 to 0.93 for that path alone.

Data Analysis

In order to determine the p_t and T_t at which the onset of condensation effects occurs along a constant M_∞ and R_c path, a data analysis procedure was developed. The main objective of the data analysis procedure was to be able to correct values of C_p on an orifice-by-orifice basis in cases where the pressure distribution over the airfoil was taken at a slightly different M_∞ than desired. With such a correction, data along the path that normally would have had to be disregarded due to small differences in M_∞ could be used. Having a more complete data base available for analysis made it easier to detect the total temperature at which differences in C_p, ΔC_p, occurred because of the effects of condensation. By examining all the orifices over the airfoil, an appropriate onset total temperature could be chosen for the airfoil as a whole. Further details of the data analysis procedure are presented in the appendix.

The Beattie-Bridgeman equation of state for gaseous nitrogen (see ref. 10) has been used to provide accurate values for the isentropic flow properties of the nitrogen gas. In unpublished studies, Adcock has shown that for isentropic flow the Beattie-Bridgeman equation gives nearly the same results as the Jacobsen equation used in reference 1.

RESULTS AND DISCUSSION

Data Presentation and Comments

The data are summarized by a series of figures for each value of M_∞ covered in this study: 0.75, 0.85, and 0.95. Each series includes averaged, condensation-free pressure distributions for each path of constant R_c, graphs showing the onset T_t for condensation effects at each orifice as a function of x/c for each path, and a summary plot for each M_∞ showing the onset conditions for each path in a plane where T_t is plotted against p_t. (All values of T_t plotted in the orifice onset graphs are rounded to the nearest 0.5 K because of the possible 0.5-K drift in tunnel total temperature during data acquisition.) The results for each value of M_∞ are then grouped together to determine whether $M_{l,max}$ or M_∞ correlates with the onset of condensation effects.

The orifice onset graphs showing the T_t at which condensation is first detected use four different symbols for four different situations. When normal onset is detected, a circle is plotted at the appropriate $x/c, T_t$ location. When no orifice onset is detected, a square is plotted at the minimum T_t at which data were taken. When excessive scatter obscures any trends, a triangle is plotted at the minimum T_t. When an orifice pressure tube develops a leak, a diamond is plotted at the minimum T_t. Also, the airfoil onset T_t shown is not taken to be an average of orifice onset T_t's but is conservatively taken to be the warmest orifice onset T_t that appears systematic. The uncertainty band about the onset T_t is drawn to include the highest value of orifice onset T_t, whether or not the deviation is systematic.

The first test described is the $M_\infty = 0.75$ test. The averaged, condensation-free pressure distributions in figures 7, 8, and 9 give the average values of C_p at each orifice with no effects of condensation present. The graphs containing orifice onset T_t plotted against x/c are shown in figures 10, 11, and 12. It is interesting to note that in figures 11 and 12 the effects of condensation are only apparent over the first half of the airfoil, which seems to downplay the importance of any condensate growth over the airfoil itself. The summary plot of onset conditions is shown in figure 13.

The pressure distributions for the five lines of constant R_c for the $M_\infty = 0.85$ test exhibit a recompression shock at $x/c = 0.65$ and are shown in figures 14, 15, 16, 17, and 18. The graphs showing orifice onset T_t as a function of x/c are shown in figures 19, 20, 21, 22, and 23. With the possible exception of figure 23, effects appear to occur at about the same T_t over the length of the airfoil. There is no obvious sensitivity to condensation effects behind the shock or, for that matter, before the shock in the region of high local Mach number. Along the $R_c = 42 \times 10^6$ path as shown in figure 23, there does appear to be possible sensitivity behind the shock location. At x/c values of 0.75 and 0.85 the onset value of T_t appeared to be 100.5 K, which is above the trend of effects occurring at about 96.0 or 96.5 K for the majority of orifices. While the onset T_t of 100.5 K may be correct, there is scatter in the plots of ΔC_p against T_t for each of the orifices that were combined to form figure 23. Because of the uncertainties involved and because of the lack of agreement between orifice onset T_t's behind the shock location at

$x/c = 0.65$ in figure 23, the airfoil onset T_t was chosen to be 98.5 K with a possible error bar extending from 96.5 to 100.5 K. The summary plot of onset conditions for the $M_\infty = 0.85$ test is given in figure 24.

The last test condition is that of $M_\infty = 0.95$. As mentioned in the section entitled "Data Sampled," the high-pressure path at $R_c = 40 \times 10^6$ is tested at $M_\infty = 0.93$ instead of at 0.95, so there is a difference in M_∞ between the first two paths and the path for $R_c = 40 \times 10^6$. The unaffected pressure distributions are shown in figures 25, 26, and 27, and the orifice onset graphs are presented in figures 28, 29, and 30. Among the onset T_t's for the $R_c = 17 \times 10^6$ path, no one area seems to be more sensitive than any other. (See fig. 28.) However, onset T_t's for the $R_c = 27 \times 10^6$ path in figure 29 may show signs of an increased sensitivity at about $x/c = 0.40$ in the region of increasing local Mach number although the trend is not conclusive. The third path at $R_c = 40 \times 10^6$, shown in figure 30, shows an apparently uniform onset T_t over the airfoil. There were no data taken along this path between $T_t = 100.5$ and 103.5 K; consequently, there is no resolution of effects between these two temperatures, and this lack of resolution may contribute to the fairly uniform distribution of onset T_t. The lack of resolution is indeed unfortunate as can be seen in figure 31 which shows no effects at $T_t = 103.5$ K but well-developed effects at 100.5 K for ΔC_p plotted against T_t for the orifice at $x/c = 0.95$. For this path, onset T_t for the airfoil is chosen to be 102.0 K with the error bar spanning 100.5 to 103.5 K. The summary plot for onset conditions for the $M_\infty = 0.95$ test is given in figure 32.

The results for all of the M_∞ tests are now grouped together to determine whether $M_{l,max}$ or M_∞ correlates with the onset of condensation effects. The question of which Mach number is important arises because of the uncertainty in the mode of nucleation taking place. This uncertainty is discussed in the next section.

The first pair of figures comparing all of the onset results is constructed for the supercooling as defined in equation (1). In equation (1), the value of T_s is the static temperature at which the isentrope, starting at the onset values of p_t and T_t, crosses the vapor-pressure curve. The value of T_e is the static temperature along the same isentrope at $M = M_{l,max}$ in figure 33(a) and at $M = M_\infty$ in figure 33(b). In both cases the value of ΔT is plotted as a function of the onset p_t for each path of contant R_c. In figure 33(a), the supercooling was nearly constant at 7 K over the pressure range for $M_\infty = 0.75$, was roughly equal to 11 K over the pressure range for $M_\infty = 0.85$, and was 12 and 14 K for the two lower pressure paths at $M_\infty = 0.95$ and then dropped to 11 K for the upper pressure path. In figure 33(b), the supercooling based on M_∞ remained between 2 and 3 K over the pressure range for both $M_\infty = 0.75$ and 0.85. However, the supercooling for the $M_\infty = 0.95$ test was 1 and 2 K for the lower pressure paths, but dropped to -1 K for the upper pressure path. Even with the behavior of the upper pressure path for the $M_\infty = 0.95$ test, there seems to be much better correlation of the values for supercooling when assuming M_∞ is the pertinent Mach number rather than $M_{l,max}$.

A second pair of figures again compares all of the onset results, but the comparison is now made in a plane where $\log_{10} p$ is plotted against T. Static values of p,T are calculated from the p_t and T_t at onset and are calcu-

lated assuming an isentropic expansion to either $M_{l,max}$ or M_∞. Figure 34(a) shows the p,T as calculated assuming $M_{l,max}$ is the Mach number of interest while figure 34(b) shows the p,T as calculated assuming M_∞ is the important Mach number. Figure 34 suggests, as does figure 33, that the onset data correlate much better with M_∞ than with $M_{l,max}$.

The seemingly early onset of effects in the upper pressure path of the $M_\infty = 0.95$ test may be the result of a tunnel configuration change that was made before the data for this path were taken. The spray-bar system used for injection of the liquid nitrogen, as described in the section "Experimental Apparatus," was removed for another investigation in the 0.3-meter tunnel. The spray-bar system remained out for the tunnel entry during which the data were obtained for the upper pressure path of the $M_\infty = 0.95$ test. With the spray bars removed, the liquid was injected from 4 nozzles flush with the interior tunnel wall at injection station 1 instead of from the 11 nozzles at the three different injection stations. Consequently, the liquid injected may not have broken up and evaporated as effectively as it did with the 11 nozzles. The additional unevaporated drops may have formed the increased number of nucleation sites necessary to decrease the amount of supercooling realized. Because of the tunnel configuration change, the data from the upper pressure path of the $M_\infty = 0.95$ test are not presented in any additional comparison graphs. Furthermore, the possible difference in effects due to differences in injection procedure would suggest that the number and location of the injection nozzle may be important factors in predicting the onset of condensation effects for different facilities.

Implications of the Data

Condensation effects can be caused by three different modes of nucleation, where nucleation is taken to mean the formation of a stable liquid droplet. The three different modes are homogeneous, heterogeneous, and binary nucleation. These three processes differ according to the manner in which they overcome an energy barrier to droplet formation and hence to droplet growth. In-depth discussion of the three types can be found in references 2 to 4 and 11 to 14. The different modes can briefly be summarized as in the following discussion.

Homogeneous nucleation can occur when the gas undergoes supercooling, a condition which will decrease the energy barrier to liquid droplet formation. When enough supercooling occurs, the gas molecules will be able to overcome the energy barrier to droplet formation, and massive nucleation rates are likely. Heterogeneous nucleation may occur when there are liquid or solid impurities suspended in the vapor at the time the flow first expands past the vapor-pressure curve and begins to supercool. The energy barrier to formation, which is so important for homogeneous condensation, is not so significant here because the impurities in the vapor can act as a catalyst for the condensation process. Consequently, little or no supercooling is needed before stable droplet growth occurs. What prevents heterogeneous nucleation from always dominating the homogeneous process is that it requires extremely large concentrations of impurity sites to influence the flow, pointed out by Oswatitsch in reference 15. The third type of nucleation possible is binary. This process occurs when a mixture of two different gases condenses into droplets which are composed of both types

of molecules. The binary process is discussed specifically in references 11 to 14. The combination of the two species can effectively change the energy barrier to nucleation so that condensation will occur earlier than analysis would predict for either of the species acting singly.

The data from the present experiment do seem to suggest which nucleation process might be taking place. First, no condensation seems to occur until at least 7 K of supercooling has taken place at the $M_{l,max}$ location. If binary nucleation takes place with some sort of impurity vapor in the nitrogen used for cooling the tunnel, then its effects are either undetectable or occur at temperatures low enough to be confused with homogeneous or heterogeneous nucleation of the nitrogen test gas. The purity of the liquid nitrogen injected for cooling is approximately 99.95 percent in the present experiments, so binary nucleation is unlikely. Second, none of the orifice onset T_t plots show any systematic trend toward condensation first appearing in the region of maximum supercooling, which is the region of high local Mach number. Since the amount of supercooling is so important for homogeneous nucleation, these results are not consistent with what one would expect if homogeneous nucleation were occurring. The effects may actually be the result of heterogeneous nucleation occurring upstream of the model in the test section. Under these circumstances the airfoil would experience the influence of these droplets over its length at about the same T_t although local sensitivity to the condensate in the free stream may vary over the airfoil because of differences in local Mach number or pressure gradient.

If condensate in the free stream causes the effects, the possible source for the impurity sites could be the injected liquid nitrogen used for cooling the tunnel. At the very low temperatures of these tests, the injected liquid may not completely evaporate in the time it takes to travel from the injection stations to the test section. (See fig. 2.) The partially evaporated droplets may provide the high concentration of nucleation sites needed for heterogeneous condensation. Some evidence for heterogeneous nucleation from unevaporated droplets in the free stream comes from figures 33 and 34. These figures show stronger correlation between the onset of effects and M_∞ than the onset of effects and $M_{l,max}$. Further evidence comes from the smaller amount of supercooling realized with the upper pressure path of the $M_\infty = 0.95$ test. Because the configuration without spray bars is less efficient at breaking up the injected liquid nitrogen, the smaller amount of supercooling seems to result from an increased number of liquid drops on which condensation growth could occur. Finally, the author's unpublished results from independent experiments using total pressure probes in the 0.3-meter tunnel support the present findings that heterogeneous nucleation occurs down the length of the test section.

Comparison to Other Works

While it appears that heterogeneous nucleation is the cause of condensation in the present experiments, most of the previous condensation investigations have concentrated on homogeneous nucleation. Some of these investigations were concerned with nitrogen gas, and two references, 16 and 17, are used here for comparison with the present data. A traditional means of presenting onset of condensation effects data is in the plane where $\log_{10} p$ is plotted against T.

As mentioned in the previous section, there is some question as to the process of nucleation and hence in the relevant condition to plot in the plane where $\log_{10} p$ is plotted against T. For the present comparisons, the static values of p and T as calculated for the $M_{l,max}$ condition were used because, regardless of the source of the effects, this amount of supercooling was realized in the region of maximum local Mach number before effects were detected.

Using the $\log_{10} p$ plotted against T format allows the present results to be compared with the analytical nitrogen-gas work done by Sivier in reference 16. His computer calculations assumed homogeneous nucleation and used classical liquid-droplet theory. A curve fit (unpublished) by Adcock to Sivier's calculated onset points for conditions of higher pressure and lower onset Mach number has been plotted together with the present onset conditions in figure 35, where Adcock's curve fit is represented by

$$\frac{1}{T_e} = 0.01461 - 0.004962 \log_{10} p + 0.0001959(\log_{10} p)^2 \qquad (2)$$

There is good agreement in trends between the curve fit to Sivier's prediction and the present results although the present onset points occur closer to the vapor-pressure curve than predicted for homogeneous nucleation. Again, heterogeneous nucleation would be consistent with the data because it would explain onset occurring before the prediction for homogeneous nucleation. However, many of the $M_\infty = 0.85$ and 0.95 onset points do approach Sivier's onset line for homogeneous nucleation. If Sivier's predictions are accurate and if heterogeneous nucleation indeed occurs in the present data, then significantly more supercooling may not be possible for the $M_\infty = 0.85$ and 0.95 tests even if the impurity sites were eliminated, since the onset line is already close to Sivier's homogeneous nucleation line.

The present results can also be compared with previous experimental results. Goglia (ref. 17) has taken data that show condensation onset in the same static pressure and temperature range as considered in the present study. When Goglia's data and the present experimental data are plotted together, as in figure 36, the agreement is especially good considering that the present results consist of subsonic and supersonic data from a 0.137-m airfoil and that Goglia's data are based on rapid expansions in a nozzle 0.114 m long at Mach numbers from 2.00 to 3.25. Although one would normally expect more supercooling with the larger velocity gradients in the nozzle, this supercooling does not appear in the data comparison. In fact, the trend of Goglia's data falls close to the present $M_\infty = 0.75$ data but seems to have somewhat less supercooling than was experienced during the present $M_\infty = 0.85$ or 0.95 tests. Goglia concludes that the condensation he detected appeared to be the result of homogeneous nucleation of the nitrogen test gas. However, the gas he used was only 95-percent-pure nitrogen and contained a 5-percent impurity of oxygen. Even though this fact was well recognized and investigated by Goglia, there may be some effects of heterogeneous nucleation on his onset points. (Arthur and Nagamatsu in ref. 6 detected a mild decrease in supercooling of about 1 to 2 K for a 5-percent oxygen impurity.)

Whether or not the condensation in the present investigation was the result of heterogeneous or homogeneous nucleation, the magnitude of the supercooling seems comparable to what others have seen or predicted in the same pressure range.

Benefits Realized

One of the primary motivations for the present experiments was to determine the increase in Reynolds number capability that might be possible when testing an airfoil with supercooled flow. This increase was determined for the NACA 0012-64 airfoil, and figure 37 shows the percent increase realized at the temperature at which condensation effects were first detected. The percent increase was calculated by dividing the R_c corresponding to p_t and T_t at onset by the R_c corresponding to p_t at onset but with a T_t which allows local saturation only. As can be seen in figure 37, the $M_\infty = 0.75$ test realized the smallest percent gain in capability at 8 percent, while the $M_\infty = 0.95$ test realized the largest at 19 percent. The $M_\infty = 0.75$ and 0.85 tests appear to show a decrease in gain with increasing p_t, while a trend for the $M_\infty = 0.95$ test cannot be predicted because of the lack of a high-pressure-path data point. Error bars shown are calculated from the uncertainty in the value of T_t for the onset of condensation effects over the airfoil.

The second motivation for the present experiment was to determine percent decreases in drive-fan power required and in the amount of liquid nitrogen (LN_2) injected when unit Reynolds number is held constant and the supercooling is used to decrease both p_t and T_t. Since the energy required for producing the amount of LN_2 injected is much greater than the energy used by the drive fan, reductions in direct operating costs while at test conditions will be much closer to the percent decrease in LN_2 required than to the decrease in drive-fan power required.

The decrease in drive-fan power realized is shown in figure 38. The trends are, of course, similar to the increase in Reynolds number capability shown in figure 37. For the $M_\infty = 0.75$ test, the decrease in drive power required remained relatively constant at 12 percent over the pressure range while for the $M_\infty = 0.85$ test, the decrease in drive power varied from 20 to 19 percent. Decreases of 23 and 24 percent were found for the two low-pressure paths in the $M_\infty = 0.95$ test. The decrease in LN_2 required to absorb drive-fan heat is shown in figure 39. (For an insulated tunnel such as the Langley 0.3-meter transonic cryogenic tunnel, the injected LN_2 required to absorb the heat flow into the tunnel through the tunnel shell insulation is relatively constant over the temperature range of the present tests and is only on the order of 1 percent of the amount required to absorb the heat of the drive fan. Consequently, heat leakage through the shell has no effect on the data described in fig. 39 and has not been included.) For the $M_\infty = 0.75$ test, the reduction in required LN_2 varied from 10 to 9 percent at the higher pressures. For $M_\infty = 0.85$, the reduction varied from 16 percent at the lower pressures to 15 percent at the higher pressures. The $M_\infty = 0.95$ test had a reduction high of 19 percent and a low of 18 percent.

CONCLUDING REMARKS

An experimental program was undertaken to determine the onset of condensation effects in the pressure distribution about a 0.137-meter NACA 0012-64 airfoil tested in the Langley 0.3-meter transonic cryogenic tunnel at free-stream Mach numbers of 0.75, 0.85, and 0.95 over a total pressure range from 1.2 to 5.0 atmospheres. Orifice pressure measurements were recorded at 5 percent chord intervals and were analyzed to determine the total temperature at which deviations first occurred in the orifice pressure coefficient.

The onset of condensation effects was found to correlate more with the amount of supercooling in the free stream than with the supercooling in the region of maximum local Mach number over the airfoil. Effects in the pressure distribution over the airfoil were generally seen to appear over its entire length at nearly the same total temperture. Both observations suggest the possibility of heterogeneous nucleation occurring in the free stream. Comparisons of the present onset results are made with calculations made by Sivier and data gathered by Goglia.

The potential operational benefits of the supercooling realized were analyzed in terms of increased Reynolds number capability at a given tunnel total pressure and reduced drive-fan power and liquid nitrogen consumption if Reynolds number is held constant. Depending on total pressure and free-stream Mach number, these three benefits are found to vary respectively from 8 to 19 percent, 12 to 24 percent, and 9 to 19 percent. Since operating costs at typical test conditions are approximately 10 percent due to drive-fan power and 90 percent due to liquid nitrogen injection, reduction in operating costs will be very close to the percentage reduction in liquid nitrogen consumption.

Although the present experimental data form a preliminary basis for predicting minimum operating temperatures for nitrogen-gas wind tunnels, it is just one of several steps that are needed for a more complete understanding of the problem. More work is needed in the following areas: tests of other airfoil pressure distributions, including angle-of-attack effects, to determine the sensitivity of the onset of condensation effects to different local velocities and gradients; experiments utilizing light scattering to follow the injected liquid nitrogen droplets around the tunnel circuit to determine whether they may be causing heterogeneous nucleation in the test section; and studies to determine scaling effects so that the present results may be extended to tunnels of other sizes.

Langley Research Center
National Aeronautics and Space Administration
Hampton, VA 23665
March 9, 1979

APPENDIX

DATA ANALYSIS AND ERROR ESTIMATES

Data Analysis Procedure

Because of the importance of the data reduction technique upon the detection of the onset of condensation effects, this section of the appendix is included in order to describe in detail the M_∞ correction procedure and to explain the procedure for determining airfoil onset T_t. Examples of the various steps are included for the $M_\infty = 0.85$ and $R_c = 16 \times 10^6$ path.

The M_∞ correction procedure is employed in order to eliminate as much as possible the effect of Mach number when C_p's are compared along a path of constant M_∞ and R_c. While M_∞ is nominally constant along a path, many pressure distributions are recorded at values of M_∞ that vary from the nominal value by ±0.010. To determine whether an M_∞ dependence exists at a given x/c location, a linear regression technique is applied to condensation-free values of C_p plotted as a function of M_∞. In this manner, if there is a correlation between C_p and M_∞, all of the data can be corrected to a single value of M_∞. If there is little or no correlation between C_p and M_∞, then a weak dependence is assumed to exist, and no correction is assumed to be necessary. Thus, all of the data along a given path of constant M_∞ and R_c can be used.

The first step of the M_∞ correction procedure is to apply a linear regression technique to condensation-free values of C_p at a given x/c as a function of M_∞. Using standard definitions, as found for example in reference 18, the slope of the linear regression fit would be given by

$$m = \frac{\sum_{i=1}^{n} \left(M_{\infty,i} - \bar{M}_\infty\right)\left(C_{p,i} - \bar{C}_p\right)}{\sum_{i=1}^{n} \left(M_{\infty,i} - \bar{M}_\infty\right)^2} \tag{A1}$$

where

$$\bar{M}_\infty = \frac{\sum_{i=1}^{n} M_{\infty,i}}{n} \tag{A2}$$

and

$$\bar{C}_p = \frac{\sum_{i=1}^{n} C_{p,i}}{n} \tag{A3}$$

The correlation coefficient r, which is an indication of goodness of fit, is given by

$$r = \frac{\sum_{i=1}^{n} \left(M_{\infty,i} - \bar{M}_\infty\right)\left(C_{p,i} - \bar{C}_p\right)}{\sqrt{\sum_{i=1}^{n} \left(M_{\infty,i} - \bar{M}_\infty\right)^2 \sum_{i=1}^{n} \left(C_{p,i} - \bar{C}_p\right)^2}} \tag{A4}$$

where if $r = 0$, there is no correlation, and if $|r| = 1$, there is perfect correlation. For the present analysis, if $|r| > 0.5$, then the correlation is considered strong enough for m to be used in correcting a given M_∞ to another value. If $|r| < 0.5$, the dependence between C_p and M_∞ is considered weak, and m is assumed to be zero. Three examples of various values of r are shown in figure 40 for the $M_\infty = 0.85$ and $R_c = 16 \times 10^6$ path. Figure 40(a) shows the linear regression fit to C_p for $x/c = 0.00$ (the orifice at the leading edge of the airfoil) as a function of M_∞. In this case $r = 0.15$ and, indeed, there seems to be little correlation between M_∞ and C_p. Consequently, no attempt is made to manipulate or correct these data for small differences in M_∞. Figure 40(b) shows the values of C_p for $x/c = 0.40$ as a function of M_∞. In this case $r = 0.49$; therefore, this linear curve fit barely fails to meet the correlation test. Figure 40(c) illustrates the values of C_p for $x/c = 0.80$ that lead to $r = 0.92$. As seen in figure 40(c), good correlation exists between C_p and M_∞, and differences in C_p due to differences in M_∞ can be removed by correcting values of C_p to a given $M_{\infty,o}$ by setting

$$C_{p,o} = C_p - m(M_\infty - M_{\infty,o}) \tag{A5}$$

where $C_{p,o}$ is the corrected value of C_p and m is the slope of the linear fit. Again, m is assumed to be equal to zero in equation (A5) if $|r| < 0.5$.

Once the linear regression technique has been applied to the values of C_p for each orifice along the path, a set of intermediate graphs is drawn before the airfoil onset T_t is determined. For each orifice a value of ΔC_p is plotted as a function of T_t where

$$\Delta C_p = C_{p,o} - C_{p,av} \tag{A6}$$

In equation (A6), $C_{p,o}$ is corrected with respect to M_∞, and $C_{p,av}$ is an average of condensation-free values of $C_{p,o}$ for that orifice. (Condensation-free values were determined by establishing crude onset values of T_t without the benefit of correction procedures; then a temperature buffer of at least a 2 K temperature was added. Final onset values of T_t were then checked to insure that $C_{p,av}$ was indeed free from condensation effects.) An example of ΔC_p plotted against T_t with and without correction is shown in figure 41 for $x/c = 0.80$ and $r = 0.92$. Figure 41(a) shows the uncorrected data and figure 41(b) shows the values of C_p after correction. As can be seen, considerable "order" is added to the data by the correction process, and this order permits easier identification of the T_t at which C_p for this x/c location begins to depart from its unaffected average value. Not always, however, was $|r| > 0.5$, and so this simplification was not always possible. Whether or not $|r| > 0.5$, graphs similar to figure 41(a) or 41(b) are then drawn for each orifice location over the airfoil. These graphs are used to determine at what T_t each of the orifices first experiences systematic departure from its unaffected average value of $C_{p,o}$.

These orifice onset temperatures are then plotted as a function of x/c as was shown in figure 19. The orifice onset plots are the key analysis graphs because they provide an overview of the effects on the airfoil as a whole. There is experimental uncertainty in the onset point for each orifice; consequently, it is helpful to see all of the orifice onset T_t's together so that a particularly low or high value can be checked for possible error. The airfoil onset T_t is not taken to be an average of orifice onset T_t's; rather it is taken to be the warmest orifice onset T_t that appears systematic. Uncertainty bars are drawn to encompass the highest orifice onset T_t, whether the deviation appears systematic or not.

The data analysis procedure described herein was more sensitive to condensation onset than previous analyses described in references 19, 20, and 21. In references 19 and 20, pressure distributions were superimposed to detect differences, but no correction was made to C_p for differences in M_∞ and, consequently, much of the data could not be used. Reference 21 used the ΔC_p plotted against T_t format at 0-, 25-, 50-, and 75-percent-chord locations but still did not include the correction technique for Mach number.

Error Estimate for Graphs With ΔC_p Plotted Against T_t

During the present experiment, fluctuations in wind-tunnel conditions were the principal source of error during the 50-sec period required to record the data. Tunnel conditions were observed to fluctuate with standard deviations of the following magnitudes: σ_{p_t} of ±0.005 atm (varied with M_∞ and R_c); σ_{M_∞} of ±0.003; and σ_{T_t} of ±0.5 K. The manufacturer's stated accuracy in the static-pressure measurements was 0.5 percent of full scale. A representative standard deviation due to these fluctuations is calculated herein for ΔC_p, as

defined in equation (A6), using normal error propagation techniques. (See ref. 22, for example.) With the terms in equation (A6) defining ΔC_p and with $C_{p,av}$ simply the average of the corrected condensation-free data, the variance of $C_{p,av}$ can be approximated by

$$\sigma^2_{C_{p,av}} = \frac{\sigma^2_{C_{p,o}}}{n - 1} \tag{A7}$$

where n would be the number of samples used in the average. The variance of $C_{p,o}$ can be written from equation (A5) as

$$\sigma^2_{C_{p,o}} = \sigma^2_{C_p} + \sigma^2_f \tag{A8}$$

where f is defined as

$$f = m(M_\infty - M_{\infty,o}) \tag{A9}$$

If there is much more relative error in $(M_\infty - M_{\infty,o})$ than in m, the variance in f results primarily from the variance in the difference in Mach numbers. Since $M_{\infty,o}$ is an arbitrarily defined constant, σ^2_f may be written

$$\sigma^2_f = m^2\sigma^2_{M_\infty} \tag{A10}$$

Consequently, equations (A5) to (A10) lead to

$$\sigma^2_{\Delta C_p} = \left(\frac{n}{n - 1}\right)\left(\sigma^2_{C_p} + m^2\sigma^2_{M_\infty}\right) \tag{A11}$$

It now remains to discuss $\sigma^2_{C_p}$, the variance associated with error in the values of C_p before the M_∞ correction procedure. C_p is defined as

$$C_p = \frac{p - p_\infty}{q_\infty} \tag{A12}$$

Although C_p is strictly a function of R_c and M_∞ as Schlichting explains in reference 23, the value of C_p calculated from an experiment may be sensitive to errors or fluctuations in p, p_t, T_t, and M_∞. In other words, one must distinguish between actual C_p,$C_{p,act}$, and calculated C_p,$C_{p,calc}$. During the present experiment, the primary difference between $C_{p,act}$ and $C_{p,calc}$ was lack of simultaneity; tunnel conditions were recorded at some time and the static value of p at an orifice may have been recorded at a time up to 50 sec later. Calculation of the impact of all the fluctuations upon the possible error in $C_{p,calc}$ are presented in the following discussion except for the dependence of $C_{p,calc}$ on T_t. Since T_t only enters the dependence of $C_{p,calc}$ through R_c and since the R_c dependence was weak, no error in C_p due to T_t was calculated. An equation for the variance of C_p can be written as

$$\sigma^2_{C_{p,calc}} = \left(\frac{\partial C_p}{\partial p_t}\right)^2 \sigma^2_{p_t} + \left(\frac{\partial C_p}{\partial M_\infty}\right)^2 \sigma^2_{M_\infty} + \left(\frac{\partial C_p}{\partial p}\right)^2 \sigma^2_p \tag{A13}$$

The next three paragraphs describe the calculation of the partial derivatives.

The calculation of the first partial derivative $\frac{\partial C_{p,calc}}{\partial p_t}$ begins with rewriting equation (A12):

$$C_{p,act} = \frac{\frac{p}{p_t} - \frac{p_\infty}{p_t}}{\frac{q_\infty}{p_t}} \tag{A14}$$

Since this derivative is calculated assuming M_∞ and R are constant, $C_{p,act}$, $\frac{p_\infty}{p_t}$, and $\frac{q_\infty}{p_t}$ remain constant even though p_t itself may change. Consequently, equation (A14) gives

$$\frac{p}{p_t} = \text{Constant} \tag{A15}$$

or

$$\left.\frac{\partial p}{\partial p_t}\right|_{M,R,x/c} = \frac{p}{p_t} \tag{A16}$$

Since the tunnel conditions p_t, p_∞, and q_∞ are recorded at some time 1 and p is recorded at some time 2, any fluctuation in $C_{p,calc}$ due to changes in p_t beween time 1 and time 2 are reflected in the value of p. With variables taken at time 1 (subscripted as a 1) and p taken at time 2 (subscripted as 2), equation (A14) can be written as

$$C_{p,calc} = \frac{\dfrac{p_2}{p_{t,1}} - \dfrac{p_{\infty,1}}{p_{t,1}}}{\dfrac{q_{\infty,1}}{p_{t,1}}} \tag{A17}$$

so that

$$\left.\frac{\partial C_{p,calc}}{\partial p_t}\right|_{M_\infty,R,x/c} = \frac{1}{q_{\infty,1}} \left.\frac{\partial p_2}{\partial p_t}\right|_{M_\infty,R,x/c} \tag{A18}$$

or combining with equation (A16) and dropping the subscripts 1 and 2 gives

$$\left.\frac{\partial C_{p,calc}}{\partial p_t}\right|_{M_\infty,R,x/c} = \frac{p}{q_\infty p_t} \tag{A19}$$

If the isentropic relation for a perfect gas with its ratio of specific heats equal to 1.4 is assumed, equation (A19) can be written as

$$\left.\frac{\partial C_{p,calc}}{\partial p_t}\right|_{M_\infty,R,x/c} = \frac{1}{p_t}\left(C_p + \frac{10}{7M_\infty^2}\right) \tag{A20}$$

APPENDIX

The partial derivative $\frac{\partial C_{p,calc}}{\partial M_\infty}$ is found when the linear regression step in the Mach correction technique is performed as described in the data analysis procedure. The value of $\frac{\partial C_{p,calc}}{\partial M_\infty}$ is equal to the value of the slope m as shown in the equation

$$\frac{\partial C_{p,calc}}{\partial M_\infty} = m \tag{A21}$$

because m is just the linear regression fit to calculated values of C_p as a function of M_∞. As before, when the correlation coefficient r does not reflect good correlation, then $\frac{\partial C_{p,calc}}{\partial M_\infty}$, like m, is assumed to be equal to zero.

The calculation of the third partial derivative $\frac{\partial C_{p,calc}}{\partial p}$ is simply where $C_{p,calc}$ is in error because of instrument error in p. Consequently,

$$\frac{\partial C_{p,calc}}{\partial p} = \frac{1}{q_\infty} \tag{A22}$$

or, in terms of M_∞ and p_t for the isentropic flow of a perfect gas with a ratio of specific heats equal to 1.4,

$$\frac{\partial C_{p,calc}}{\partial p} = \frac{10\left(1 + \frac{M_\infty^2}{5}\right)^{3.5}}{7p_t M_\infty^2} \tag{A23}$$

At this point, all of the partial derivatives in equation (A13) are known and can be combined with the observed or known values of σ_{p_t}, σ_{M_∞}, and σ_p. The value of σ_p was first taken to be the manufacturer's value for accuracy

of 0.5 percent of full scale, but this value gave a contribution to the error bar in C_p on the order of 10 times the actual fluctuations in C_p. What was needed for the purpose of differentiating between condensation-induced and random deviations in C_p was σ_p based on transducer precision. Consequently, instead of basing σ_p on the stated accuracies of 0.0170 and 0.0085 atm for the two transducers used, the values of σ_p were based on the observed two precisions of 0.0004 and 0.0002 atm. These low magnitudes in σ_p made the contribution of the instrument error to the total error negligible.

If isentropic relations for a perfect gas with the ratio of specific heats equal to 1.4 are assumed and if σ_p is negligible, equations (A11), (A13), (A20), and (A21) can be combined to give

$$\sigma^2_{\Delta C_p} = \left(\frac{n}{n-1}\right)\left\{\left[\left(C_p + \frac{10}{7M_\infty^2}\right)\Big/ p_t\right]^2 \sigma^2_{p_t} + 2m^2\sigma^2_{M_\infty}\right\} \tag{A24}$$

The error bars used in the graphs in the data analysis procedure where ΔC_p is plotted against T_t were calculated with the value of $\sigma_{\Delta C_p}$ just given.

REFERENCES

1. Adcock, Jerry B.: Real-Gas Effects Associated With One-Dimensional Transonic Flow of Cryogenic Nitrogen. NASA TN D-8274, 1976.

2. Wegener, P. P.; and Mach, L. M.: Condensation in Supersonic and Hypersonic Wind Tunnels. Advances in Applied Mechanics, Volume V, H. L. Dryden and Th. von Kármán, eds., Academic Press, 1958, pp. 307-447.

3. Wegener, P. P.: Nonequilibrium Flow With Condensation. Acta Mech. vol. XXI, no. 1-2, 1975, pp. 65-91.

4. Daum, Fred L.; and Gyarmathy, George: Condensation of Air and Nitrogen in Hypersonic Wind Tunnels. AIAA J., vol. 6, no. 3, Mar. 1968, pp. 458-465.

5. Goglia, Gennaro L.; and Van Wylen, Gordon J.: Experimental Determination of Limit of Supersaturation of Nitrogen Vapor Expanding in a Nozzle. Trans. ASME, Ser. C: J. Heat Transfer, vol. 83, no. 1, Feb. 1961, pp. 27-32.

6. Arthur, P. D.; and Nagamatsu, H. T.: Effects of Impurities on the Supersaturation of Nitrogen in a Hypersonic Nozzle. Memo. No. 7 (Contract No. DA-04-495-Ord-19), GALCIT, Mar. 1, 1952.

7. Adcock, Jerry B.; and Ogburn, Marilyn E.: Power Calculations for Isentropic Compressions of Cryogenic Nitrogen. NASA TN D-8389, 1977.

8. Kilgore, Robert Ashworth: The Cryogenic Wind Tunnel for High Reynolds Number Testing. Ph. D. Thesis, Univ. of Southampton, 1974. (Available as NASA TM X-70207.)

9. Kilgore, Robert A.: Design Features and Operational Characteristics of the Langley Pilot Transonic Cryogenic Tunnel. NASA TM X-72012, 1974.

10. Beattie, James A.; and Bridgeman, Oscar C.: A New Equation of State for Fluids. II. Application to Helium, Neon, Argon, Hydrogen, Nitrogen, Oxygen, Air and Methane. J. American Chem. Soc., vol. 50, no. 12, Dec. 1928, pp. 3133-3138.

11. Stauffer, D.: Kinetic Theory of Two-Component ("Heteromolecular") Nucleation and Condensation. J. Aerosol Sci., vol. 7, no. 4, July 1976, pp. 319-333.

12. Wegener, Peter P.; and Wu, Benjamin J. C.: Homogeneous and Binary Nucleation: New Experimental Results and Comparisons With Theory. Faraday Discuss. Chem. Soc., No. 61, 1976, pp. 77-82.

13. Wilemski, Gerald: Binary Nucleation. I. Theory Applied to Water-Ethanol Vapors. J. Chem. Phys., vol. 62, no. 9, May 1, 1975, pp. 3763-3771.

14. Wilemski, Gerald: Binary Nucleation. II. Time Lags. J. Chem. Phys., vol. 62, no. 9, May 1, 1975, pp. 3772-3776.

15. Oswatitsch, Kl. (M. Flint, transl.): Condensation Phenomena in Supersonic Nozzles. R.T.P. Transl. No. 1905, British Min. Aircraft Prod. (From Z. Angew. Math. & Mech., vol. 22, no. 1, Feb. 1942, pp. 1-14.)

16. Sivier, Kenneth D.: Digital Computer Studies of Condensation in Expanding One-Component Flows. ARL 65-234, U.S. Air Force, Nov. 1965. (Available from DDC as AD 628 543.)

17. Goglia, Gennaro Louis: Limit of Supersaturation of Nitrogen Vapor Expanding in a Nozzle. Ph. D. Diss., Univ. of Michigan, 1959.

18. Freund, John E.: Mathematical Statistics. Second ed. Prentice-Hall, Inc., c.1971.

19. Hall, Robert M.: Preliminary Study of the Minimum Temperatures for Valid Testing in a Cryogenic Wind Tunnel. NASA TM X-72700, 1975.

20. Hall, Robert M.; and Ray, Edward J.: Investigation of Minimum Operating Temperatures for Cryogenic Wind Tunnels. J. Aircr., vol. 14, no. 6, June 1977, pp. 560-564.

21. Hall, Robert M.: An Analysis of Data Related to the Minimum Temperatures for Valid Testing in Cryogenic Wind Tunnels Using Nitrogen as the Test Gas. NASA TM X-73924, 1976.

22. Crandall, Keith C.; and Seabloom, Robert W.: Engineering Fundamentals in Measurements, Probability, Statistics, and Dimensions. McGraw-Hill Book Co., c.1970.

23. Schlichting, Hermann (J. Kestin, transl.): Boundary-Layer Theory. Sixth ed. McGraw-Hill Book Co., Inc., c.1968.

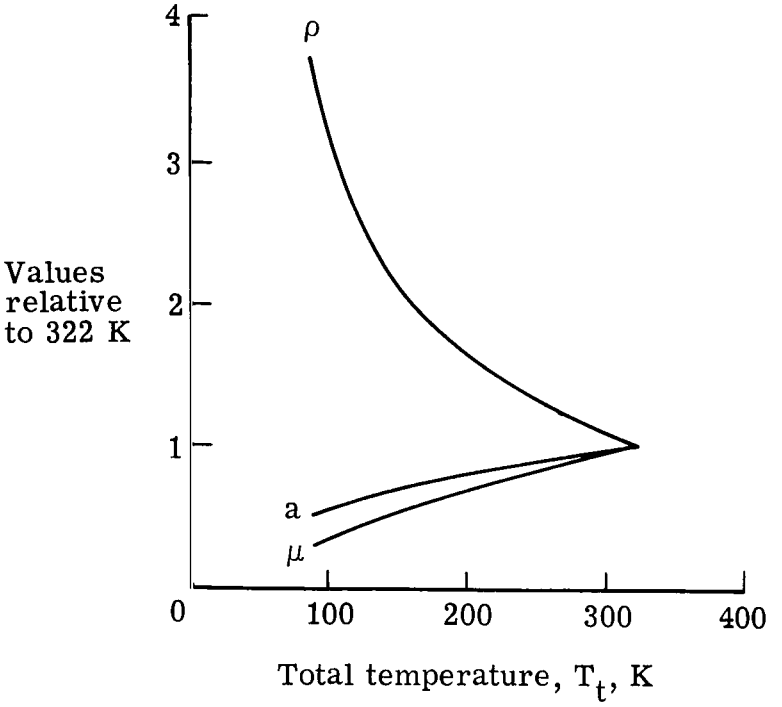

(a) Gas properties.

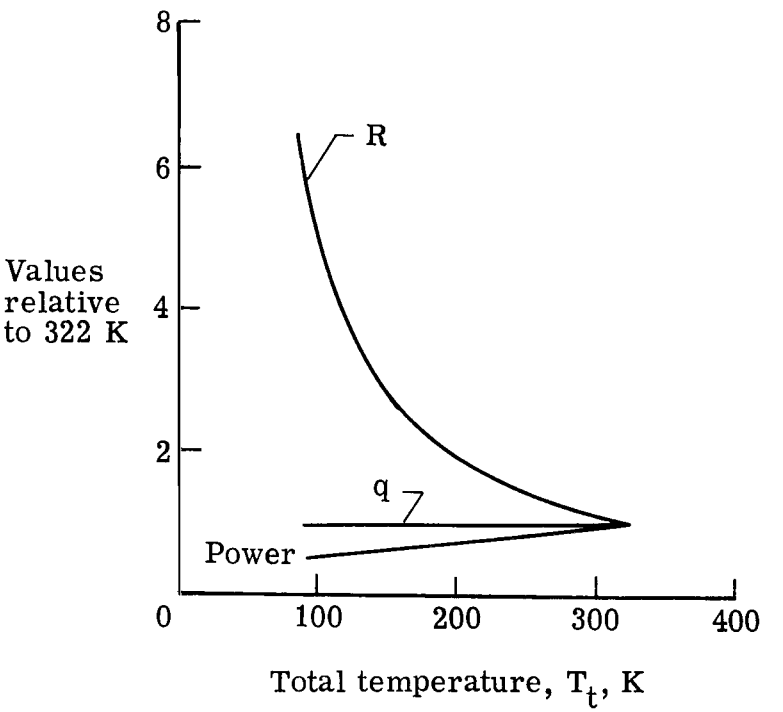

(b) Test conditions and drive power.

Figure 1.- Effect of temperature reduction for $M_\infty = 1.0$, $p_t = 1$ atm, and constant reference length.

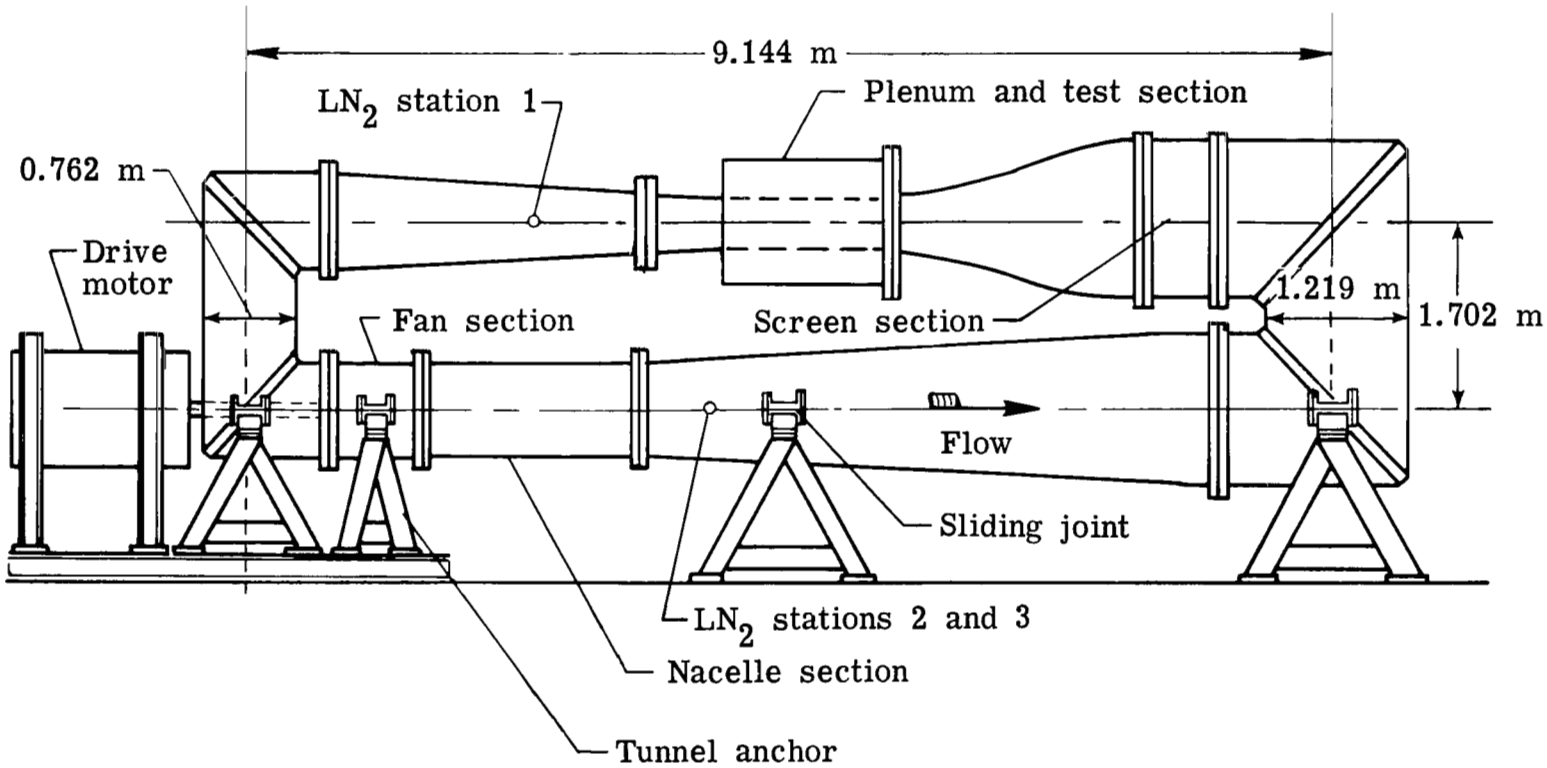

Figure 2.- Schematic of Langley 0.3-meter transonic cryogenic tunnel.

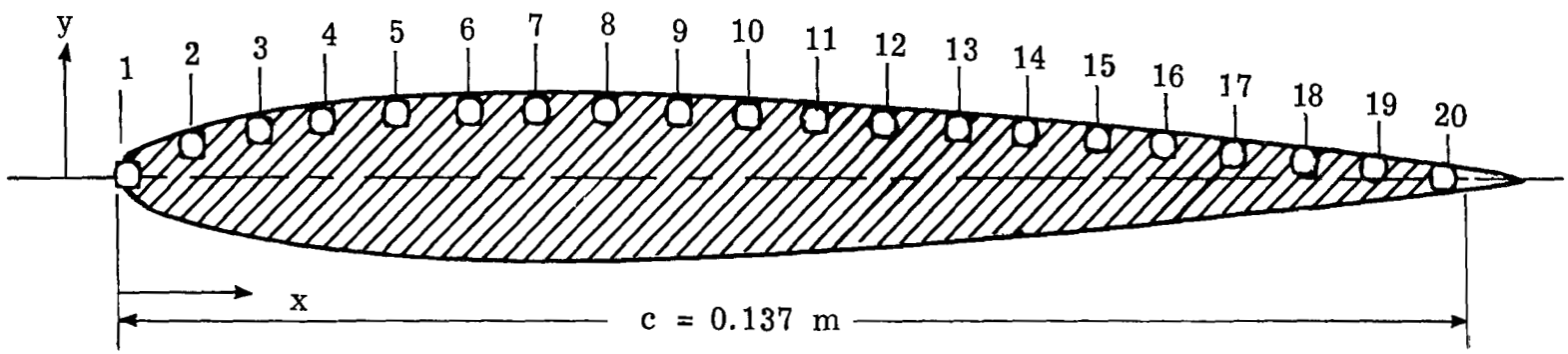

Figure 3.- Two-dimensional NACA 0012-64 airfoil with orifices spaced at 5-percent-chord locations. Trailing-edge orifice was added for tests with M_∞ = 0.75 and 0.95.

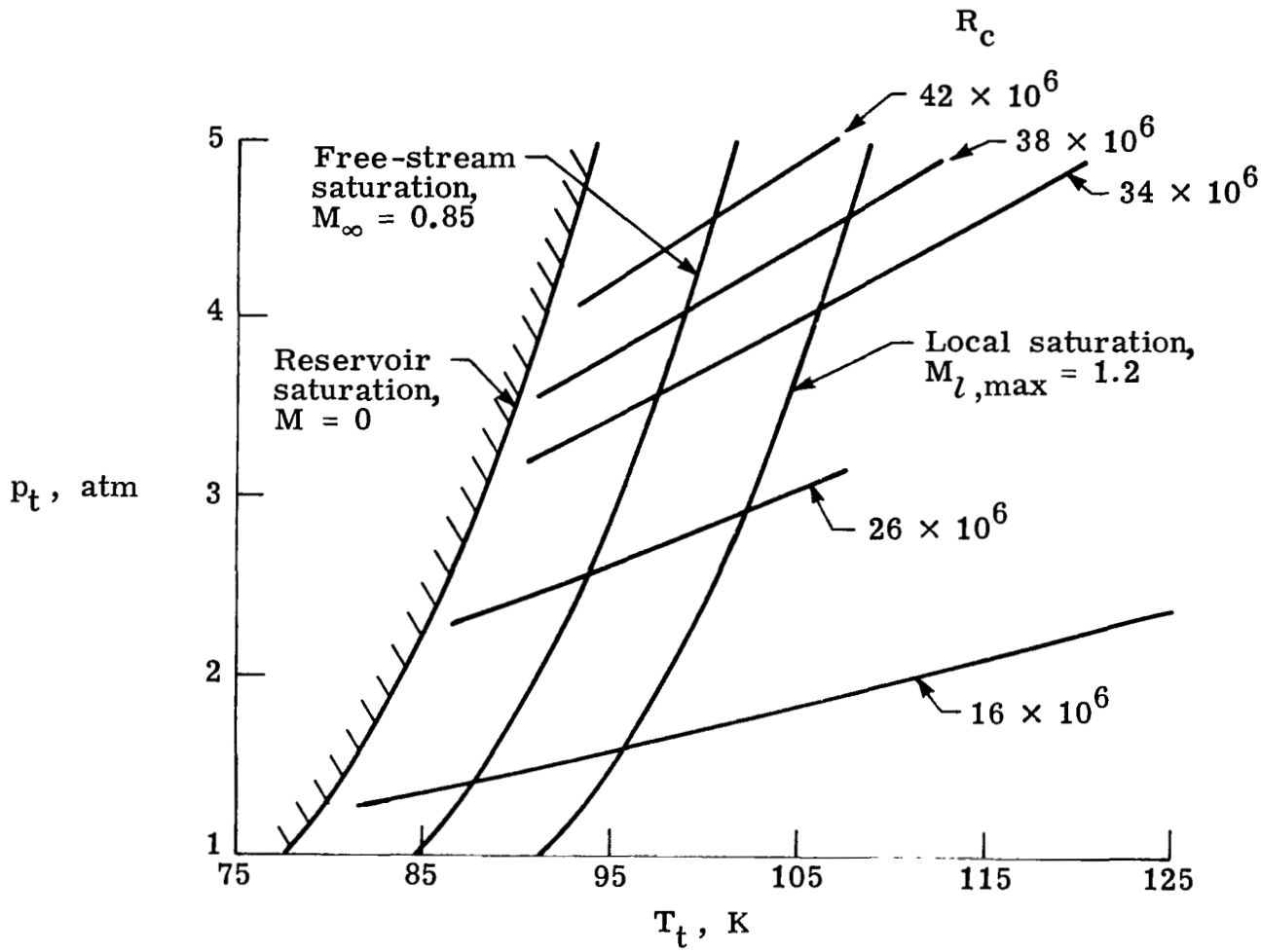

Figure 4.- Five paths of constant R_c for $M_\infty = 0.85$ test.

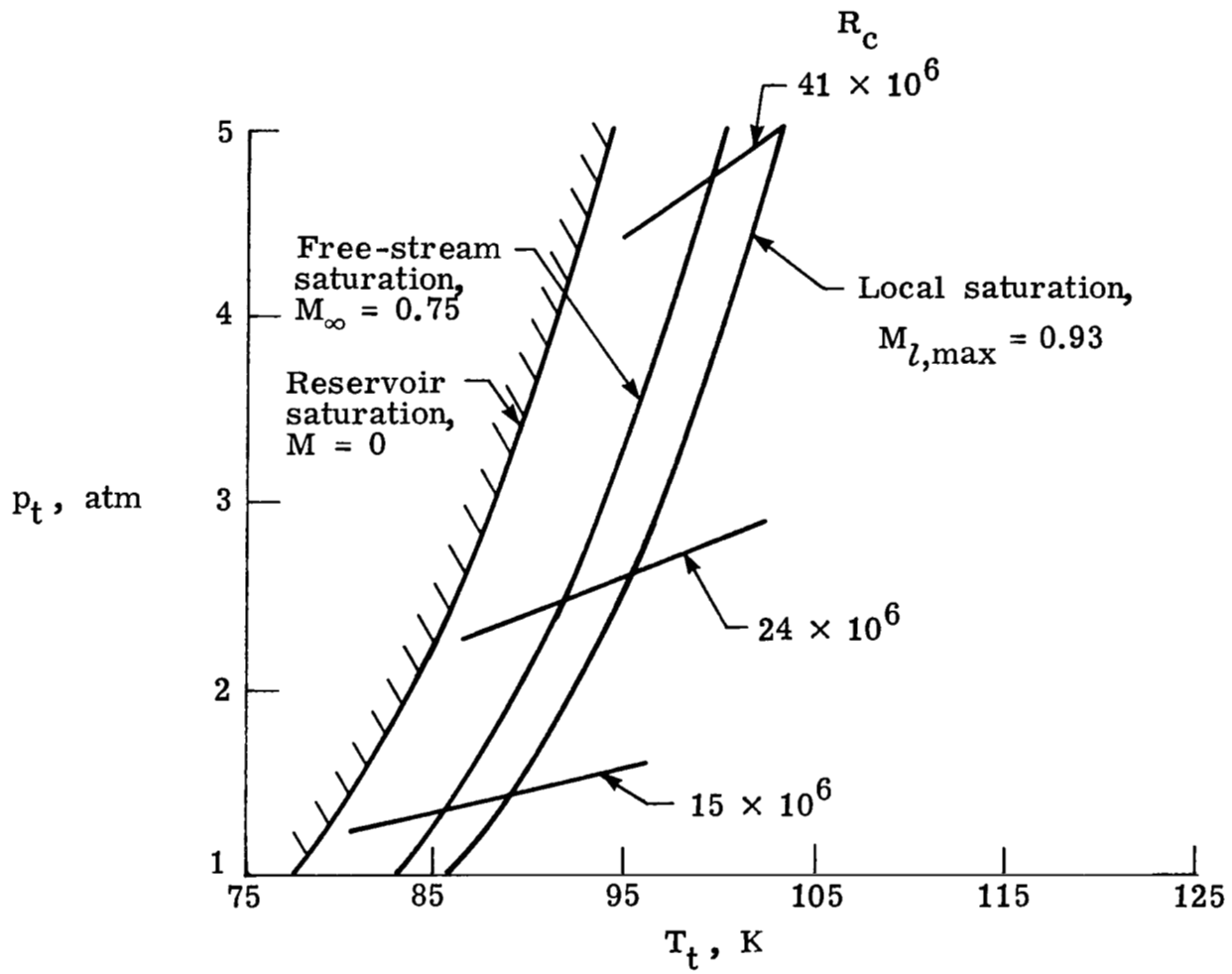

Figure 5.- Three paths of constant R_c for $M_\infty = 0.75$ test.

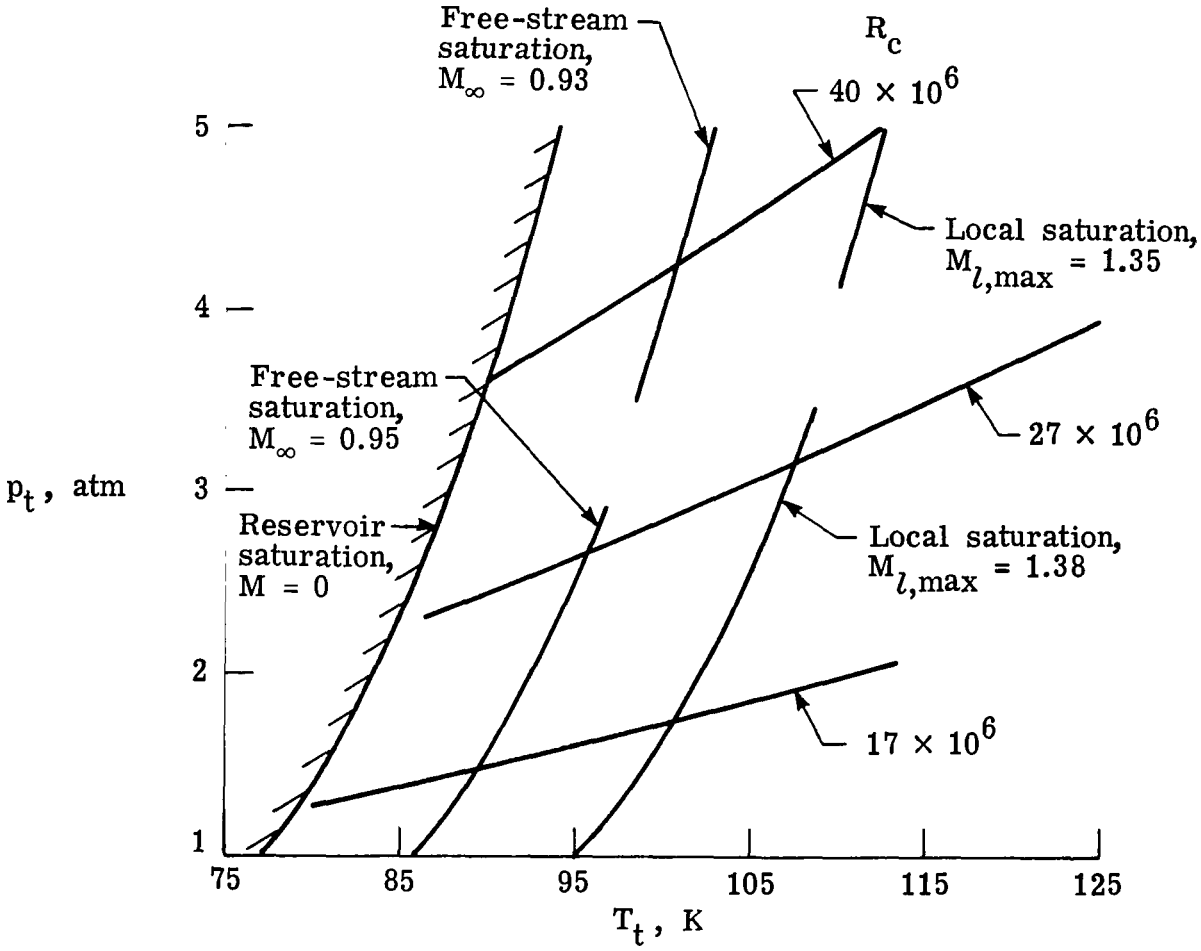

Figure 6.- Three paths of constant R_c for M_∞ = 0.95 test. (R_c = 40 × 10^6 path taken with M_∞ = 0.93.)

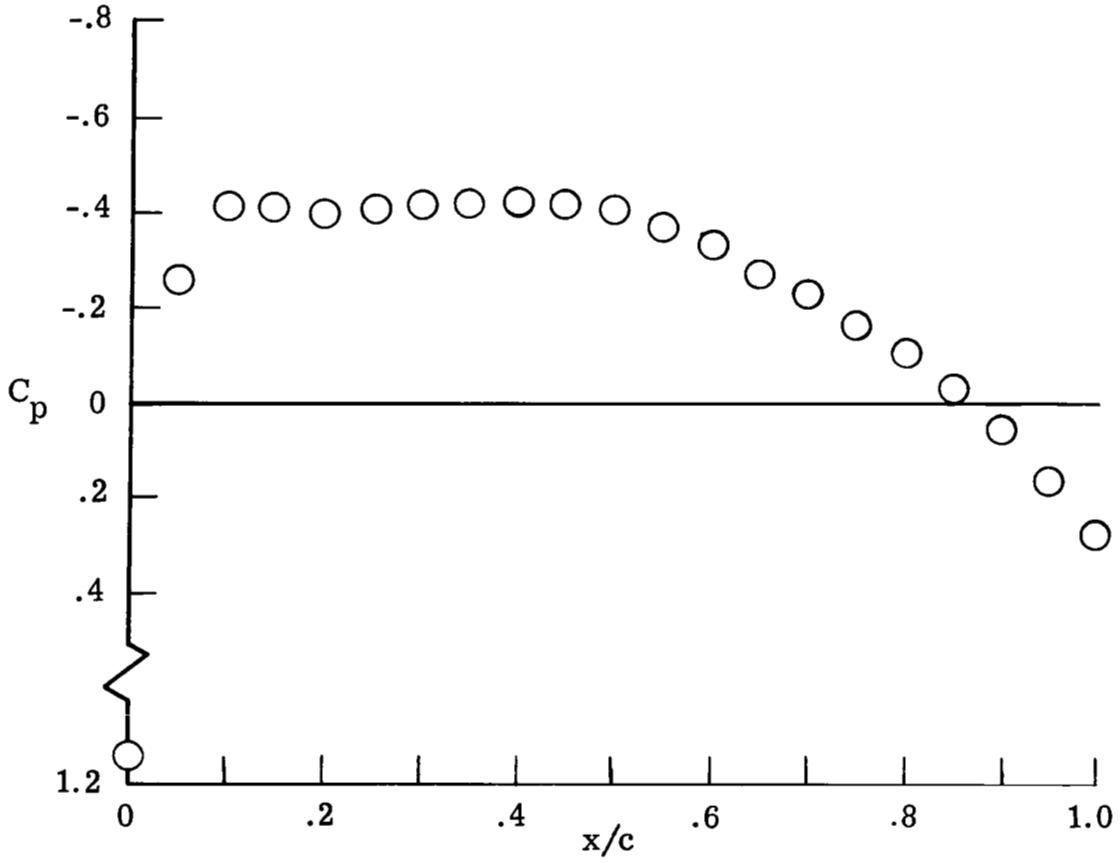

Figure 7.- Average unaffected pressure distribution for $R_c = 15 \times 10^6$ path of $M_\infty = 0.75$ test.

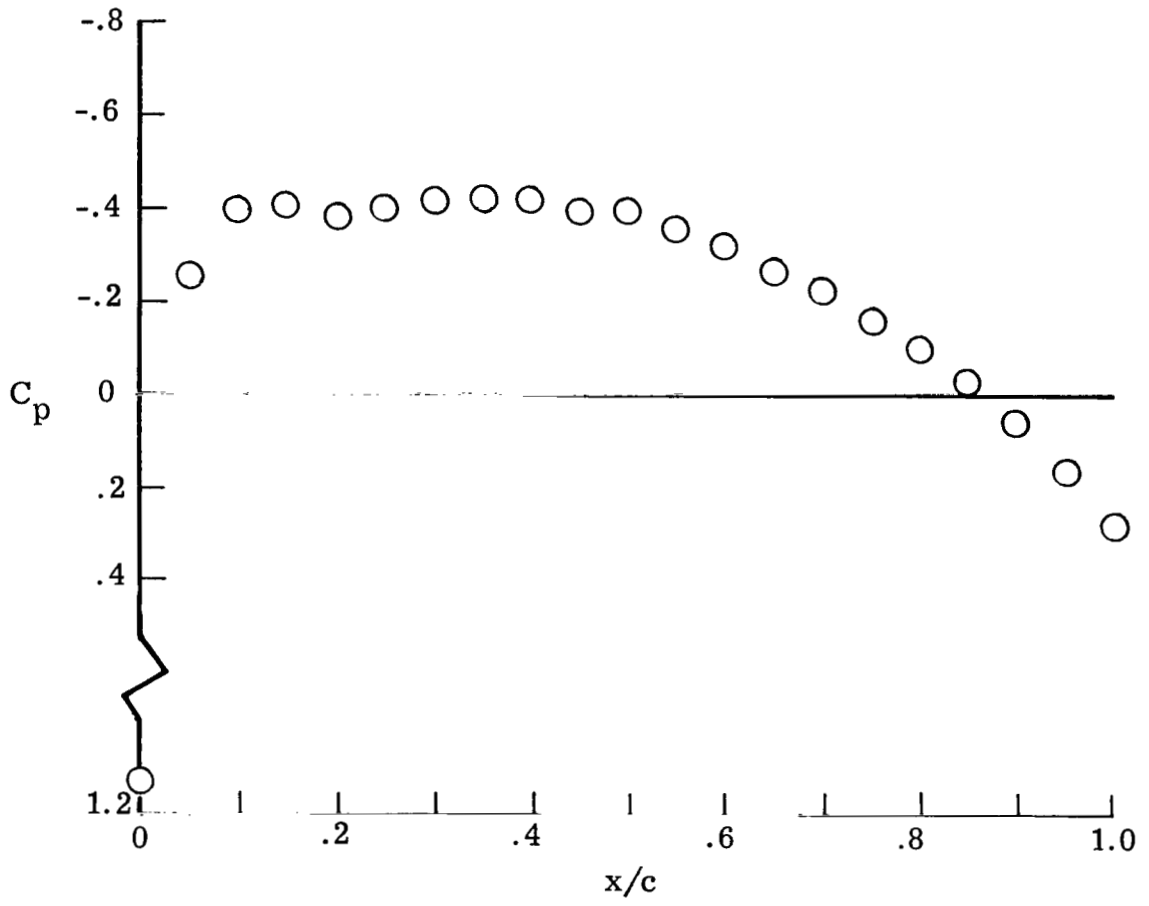

Figure 8.- Average unaffected pressure distribution for $R_c = 24 \times 10^6$ path of $M_\infty = 0.75$ test.

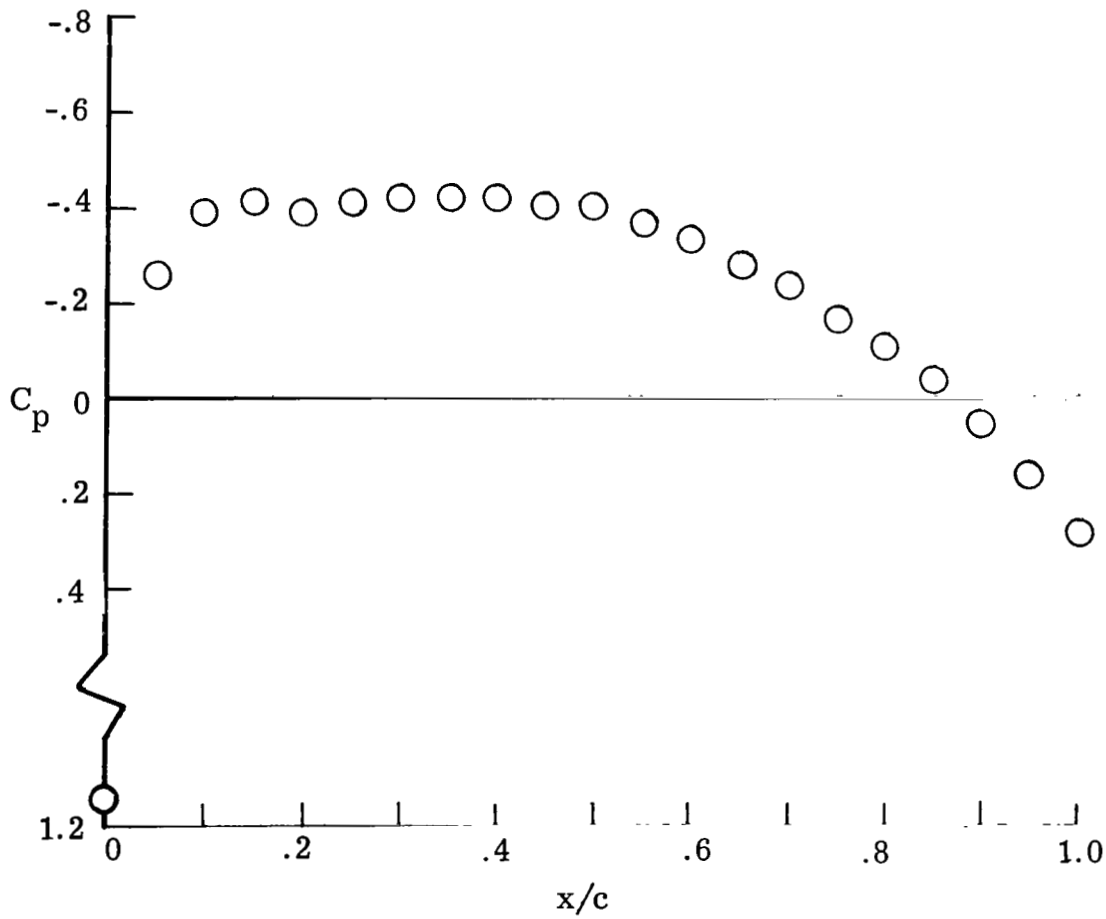

Figure 9.- Average unaffected pressure distribution for $R_C = 41 \times 10^6$ path of $M_\infty = 0.75$ test.

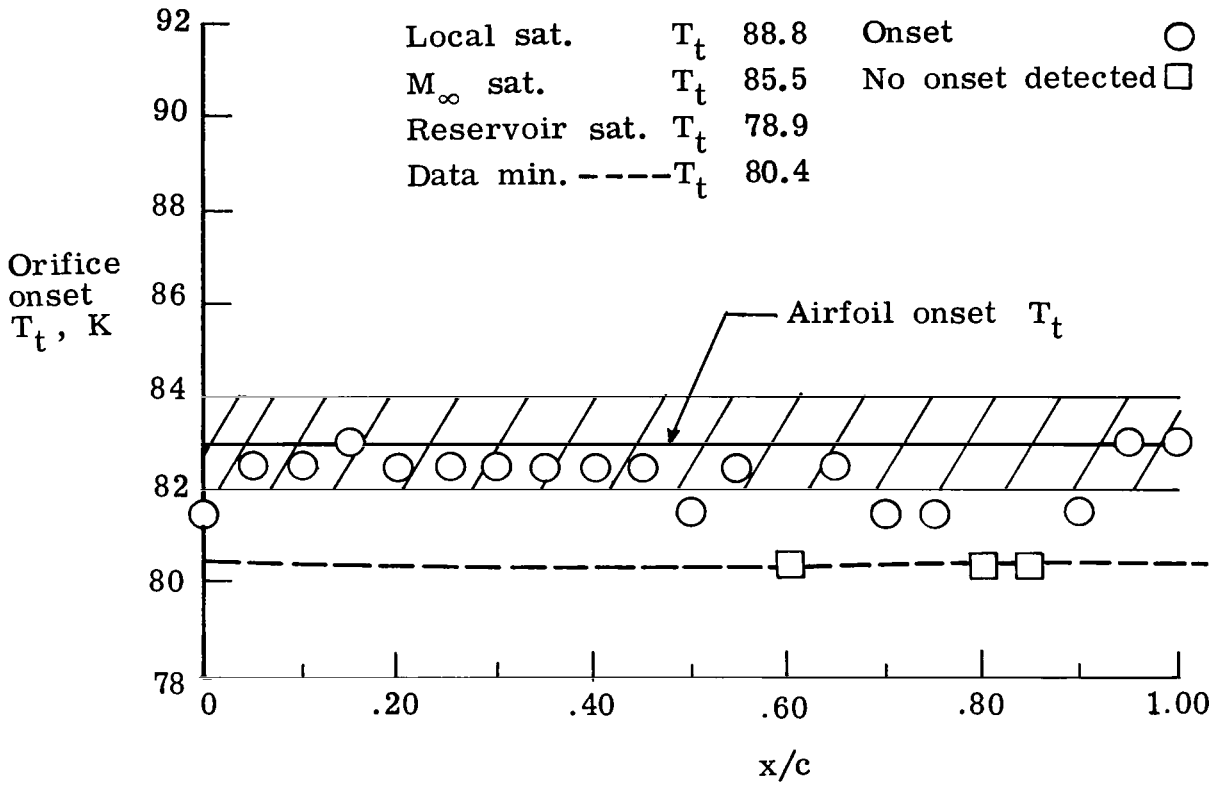

Figure 10.- Orifice onset T_t's and resulting airfoil onset T_t for $R_c = 15 \times 10^6$ path of $M_\infty = 0.75$ test.

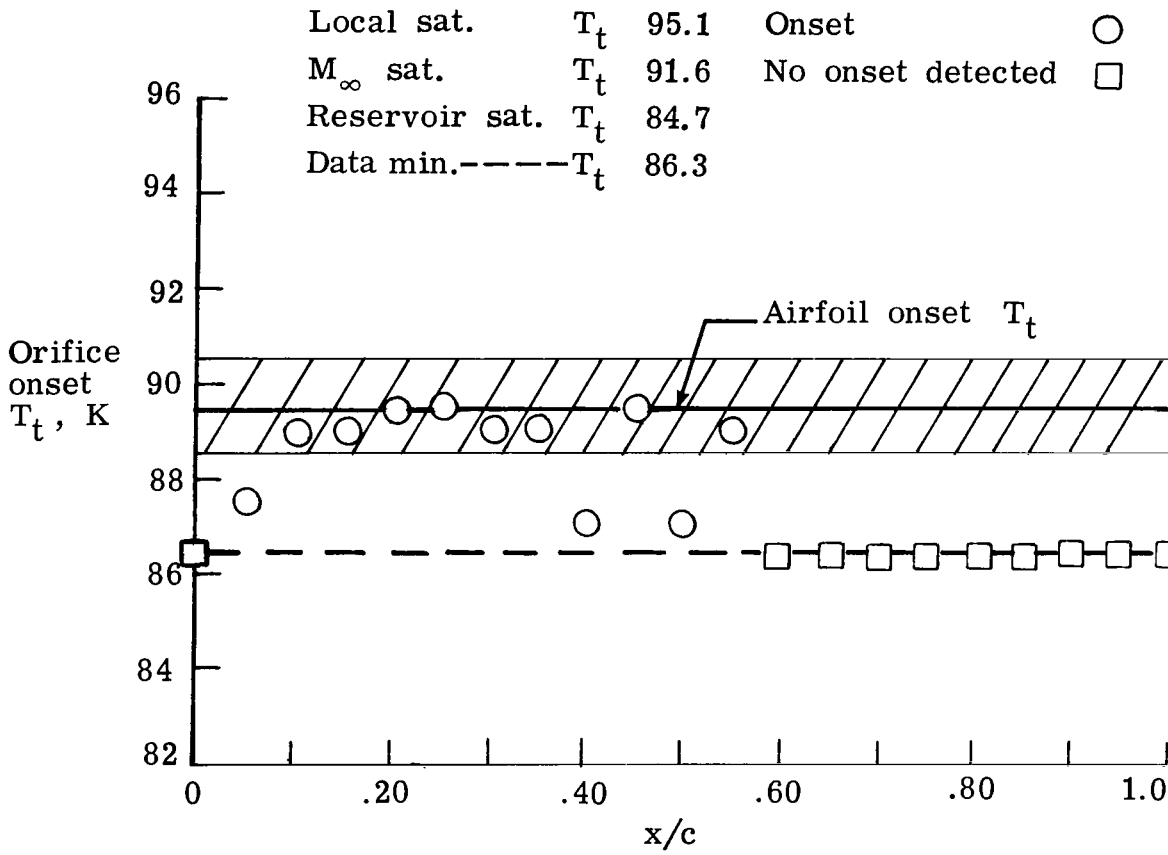

Figure 11.- Orifice onset T_t's and resulting airfoil onset T_t for $R_c = 24 \times 10^6$ path of $M_\infty = 0.75$ test.

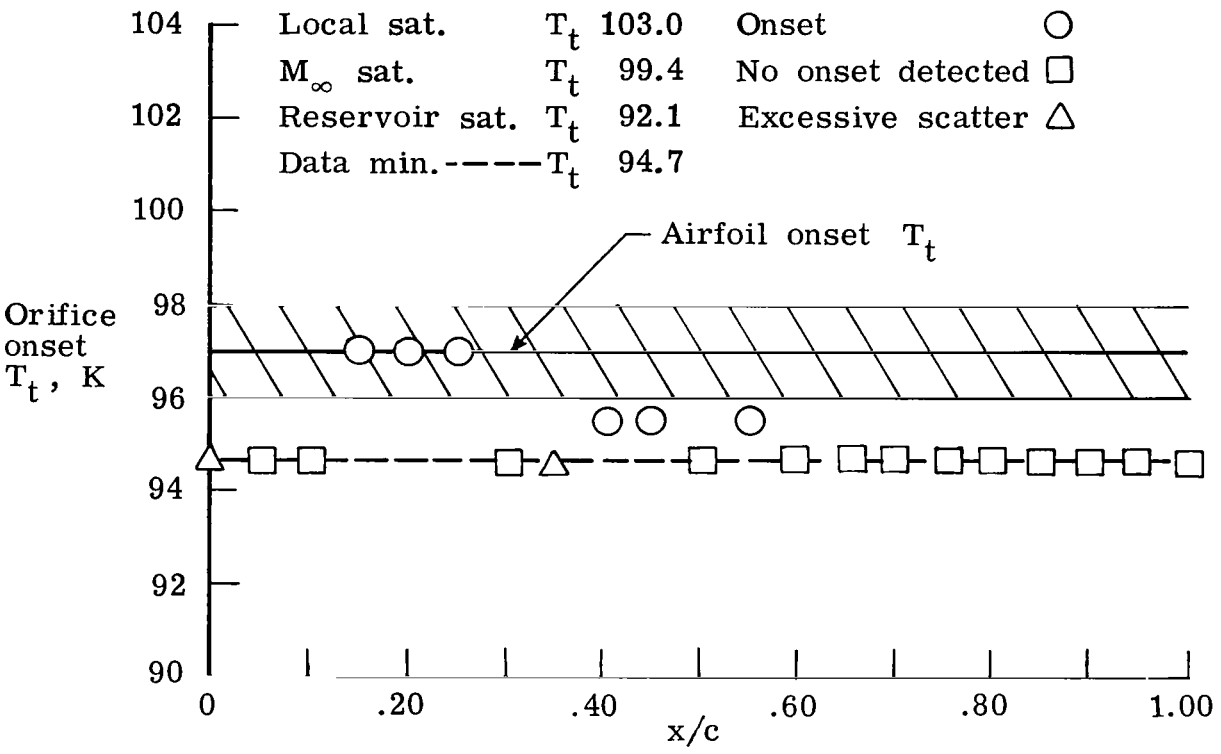

Figure 12.- Orifice onset T_t's and resulting airfoil onset T_t for $R_c = 41 \times 10^6$ path of $M_\infty = 0.75$ test.

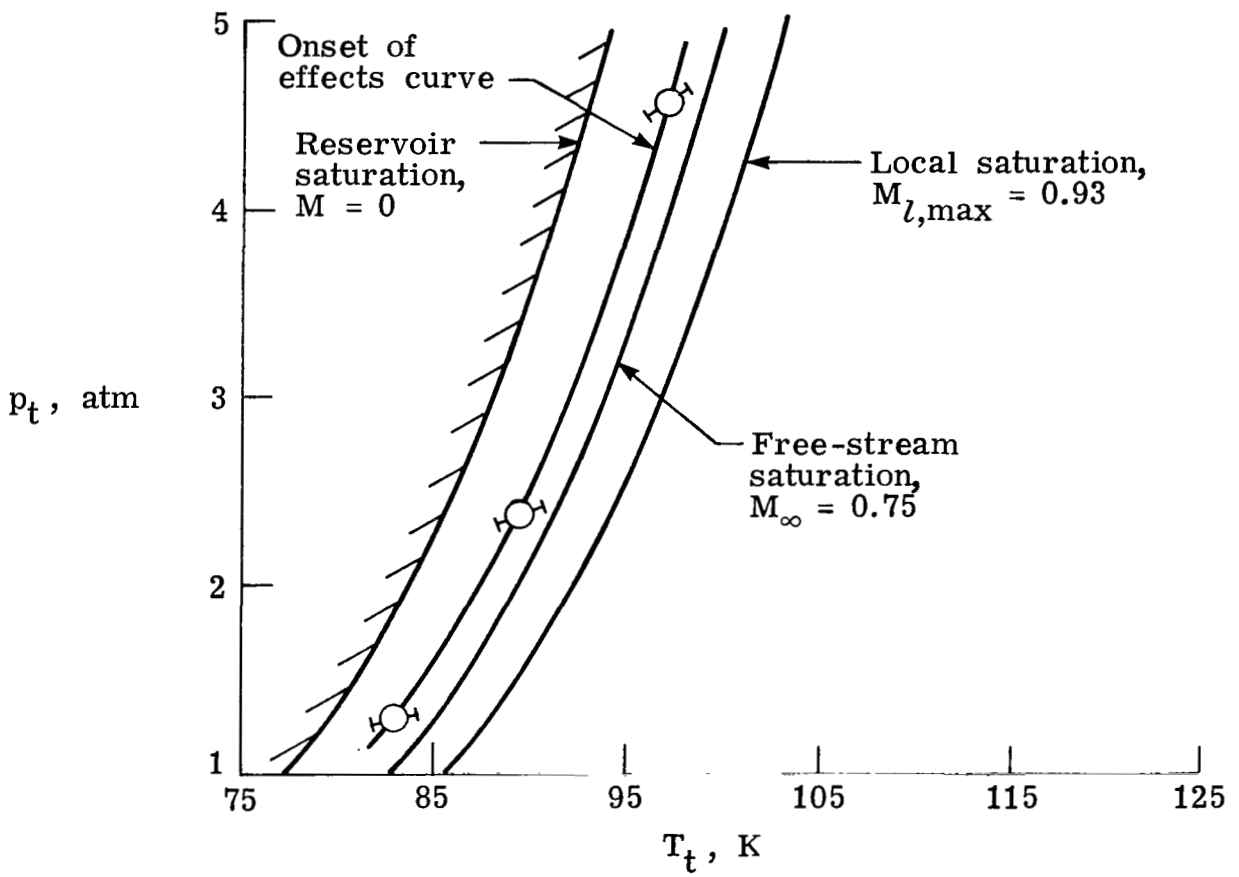

Figure 13.- Onset of condensation effects for $M_\infty = 0.75$ test. Error bars shown indicate possible experimental error.

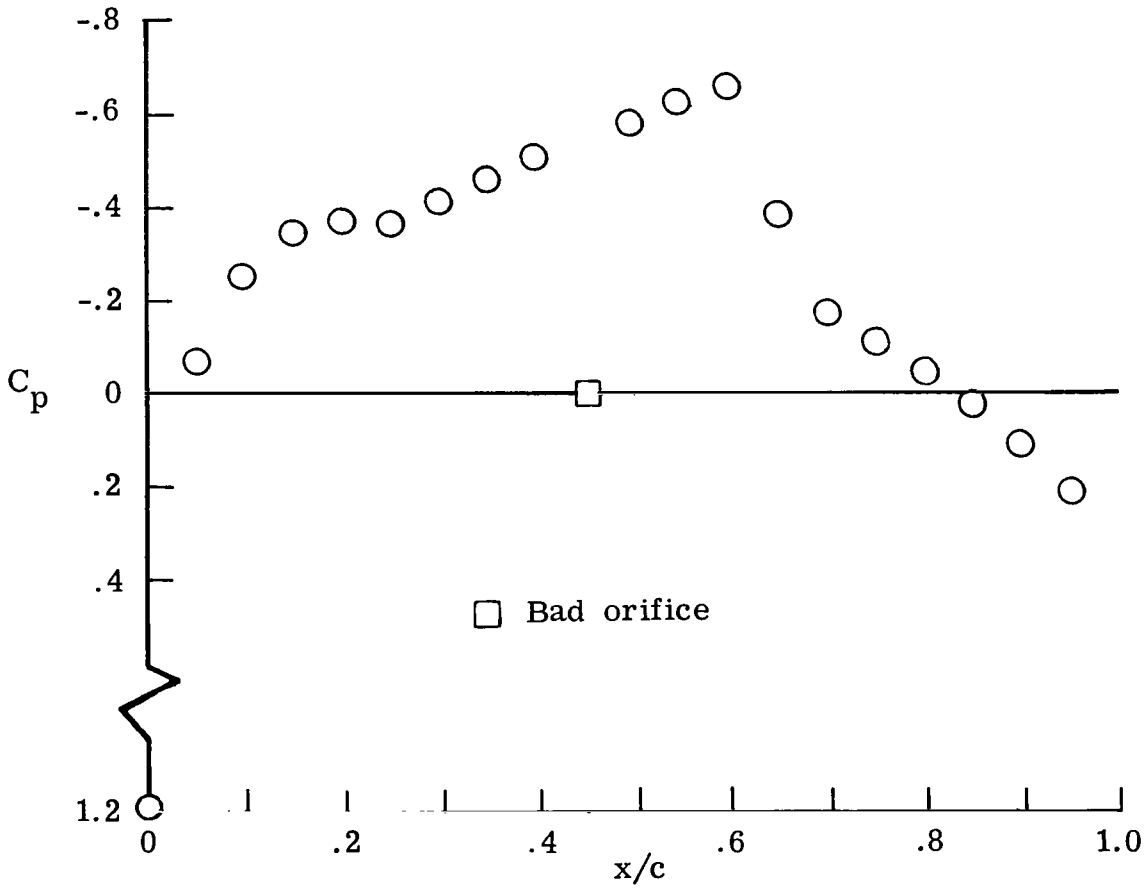

Figure 14.- Average unaffected pressure distribution for $R_c = 16 \times 10^6$ path of $M_\infty = 0.85$ test.

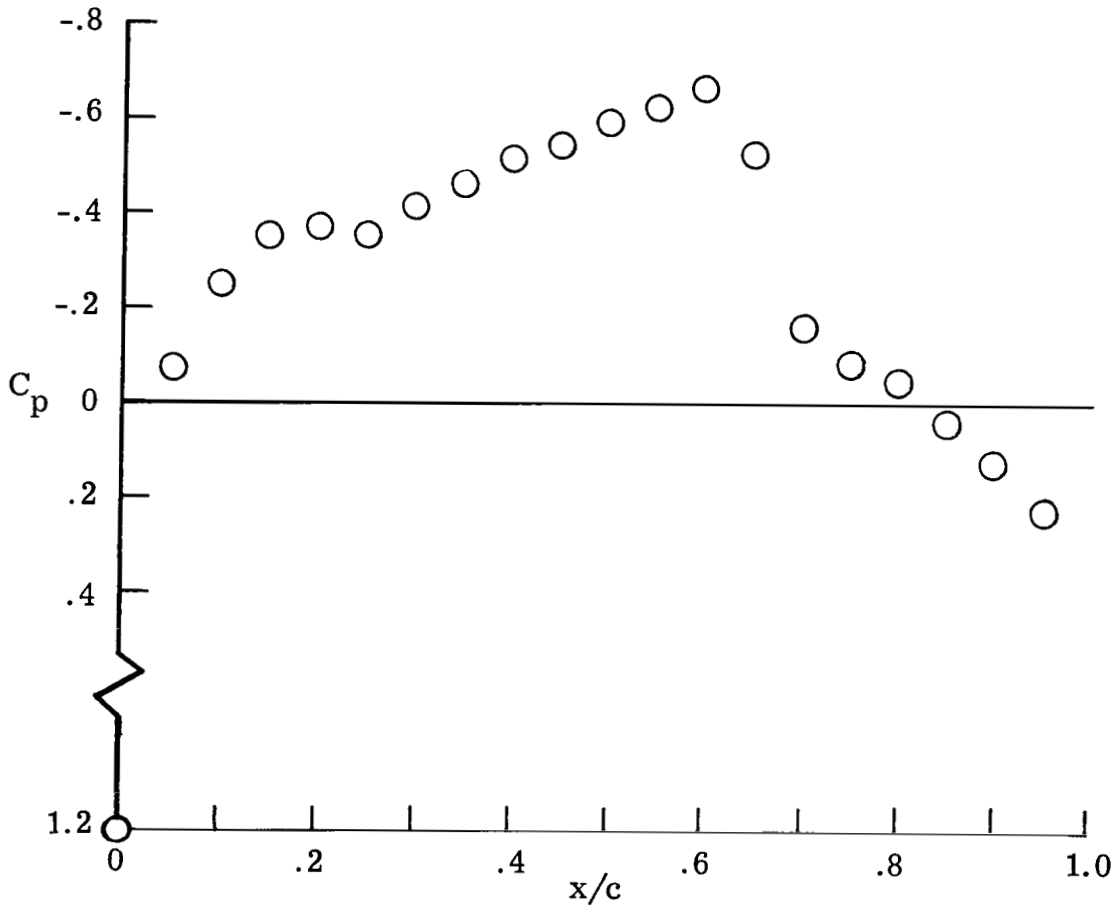

Figure 15.- Average unaffected pressure distribution for $R_c = 26 \times 10^6$ path of $M_\infty = 0.85$ test.

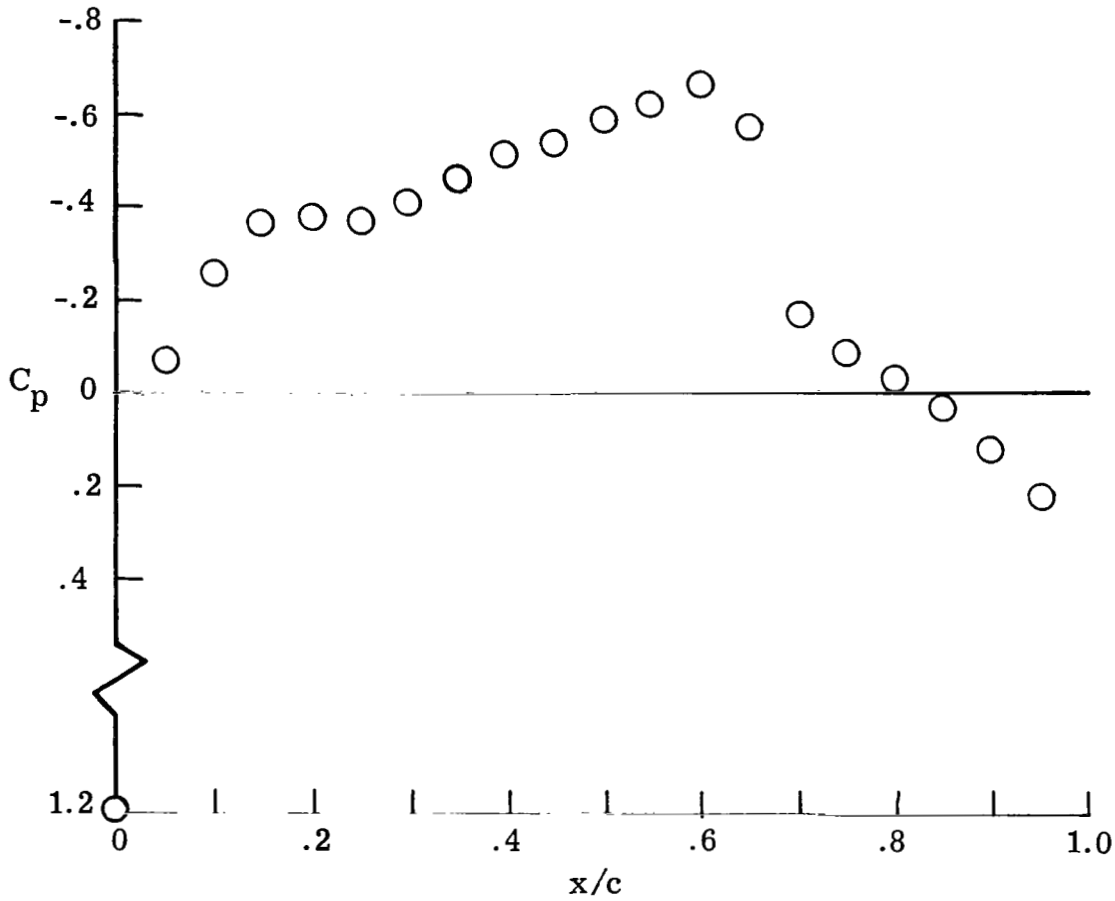

Figure 16.- Average unaffected pressure distribution for $R_c = 34 \times 10^6$ path of $M_\infty = 0.85$ test.

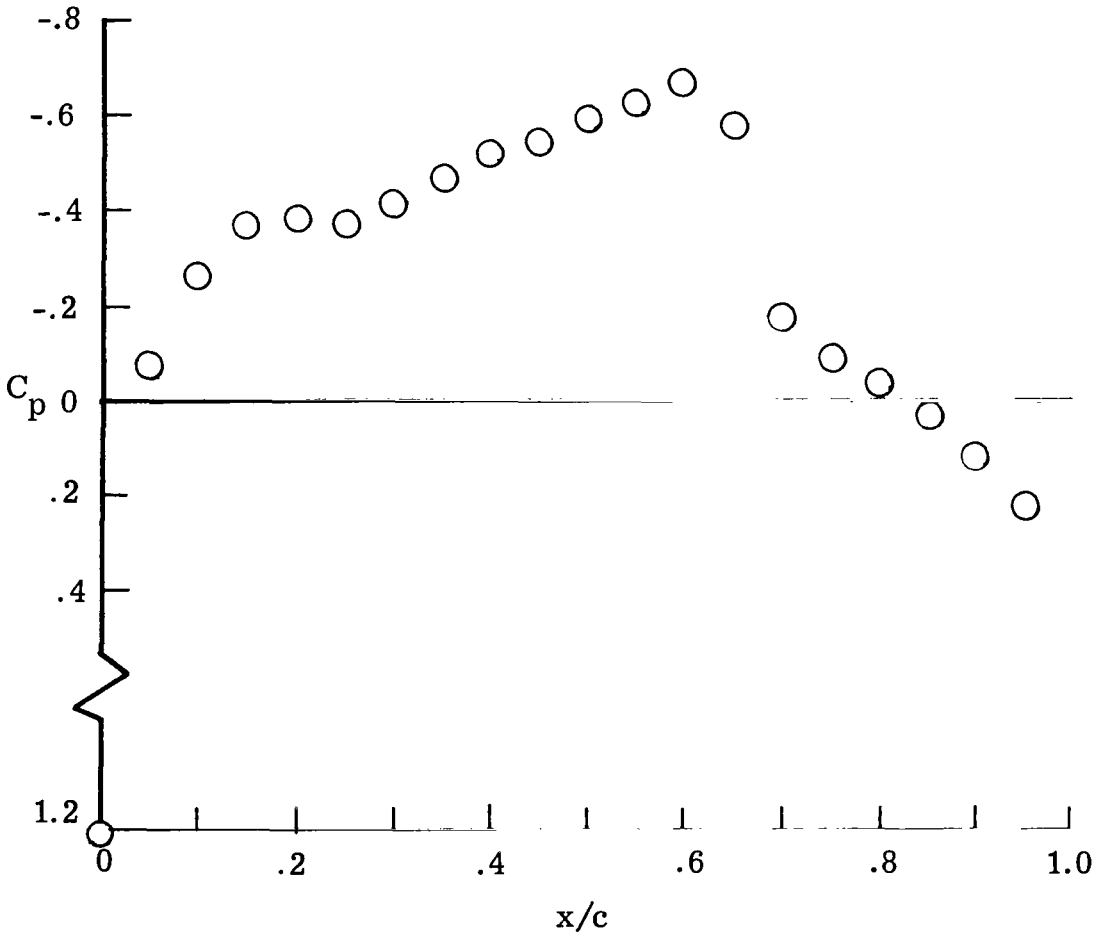

Figure 17.- Average unaffected pressure distribution for $R_c = 38 \times 10^6$ path of $M_\infty = 0.85$ test.

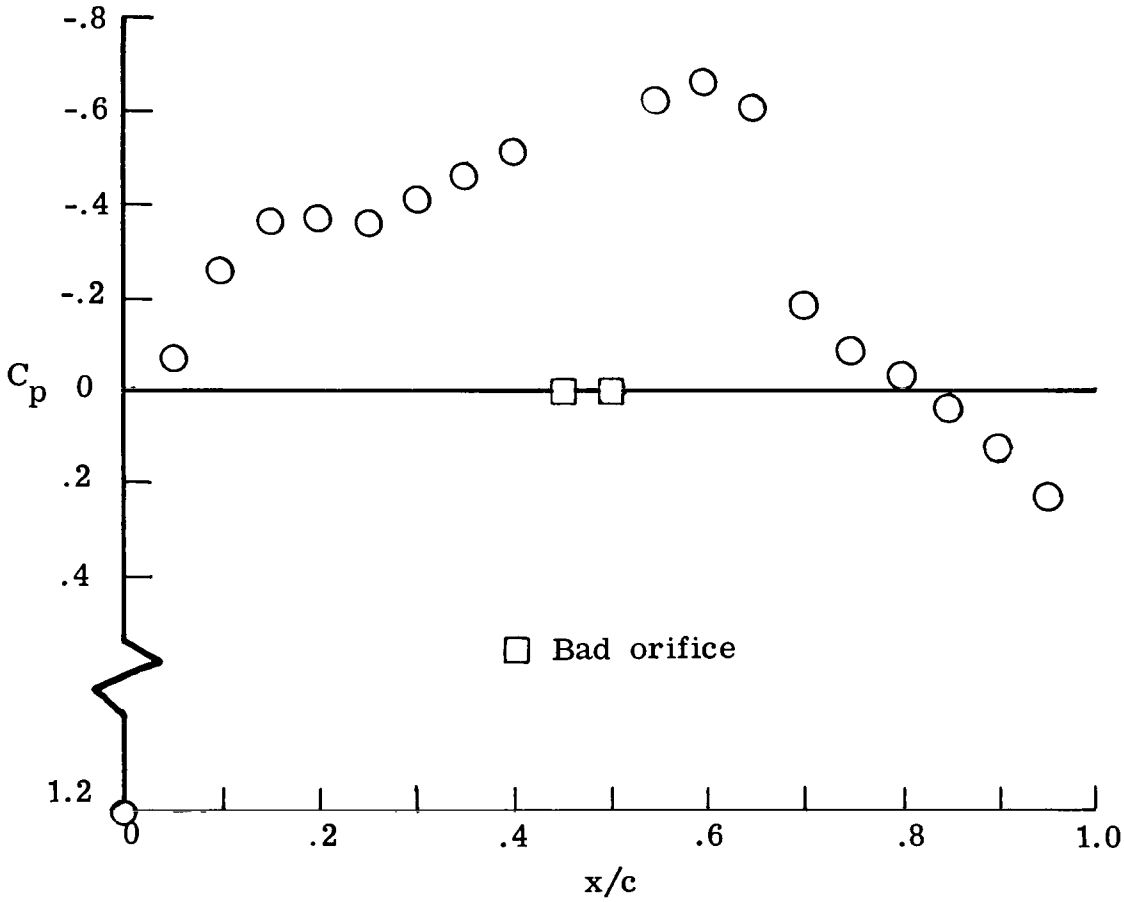

Figure 18.- Average unaffected pressure distribution for $R_c = 42 \times 10^6$ path of $M_\infty = 0.85$ test.

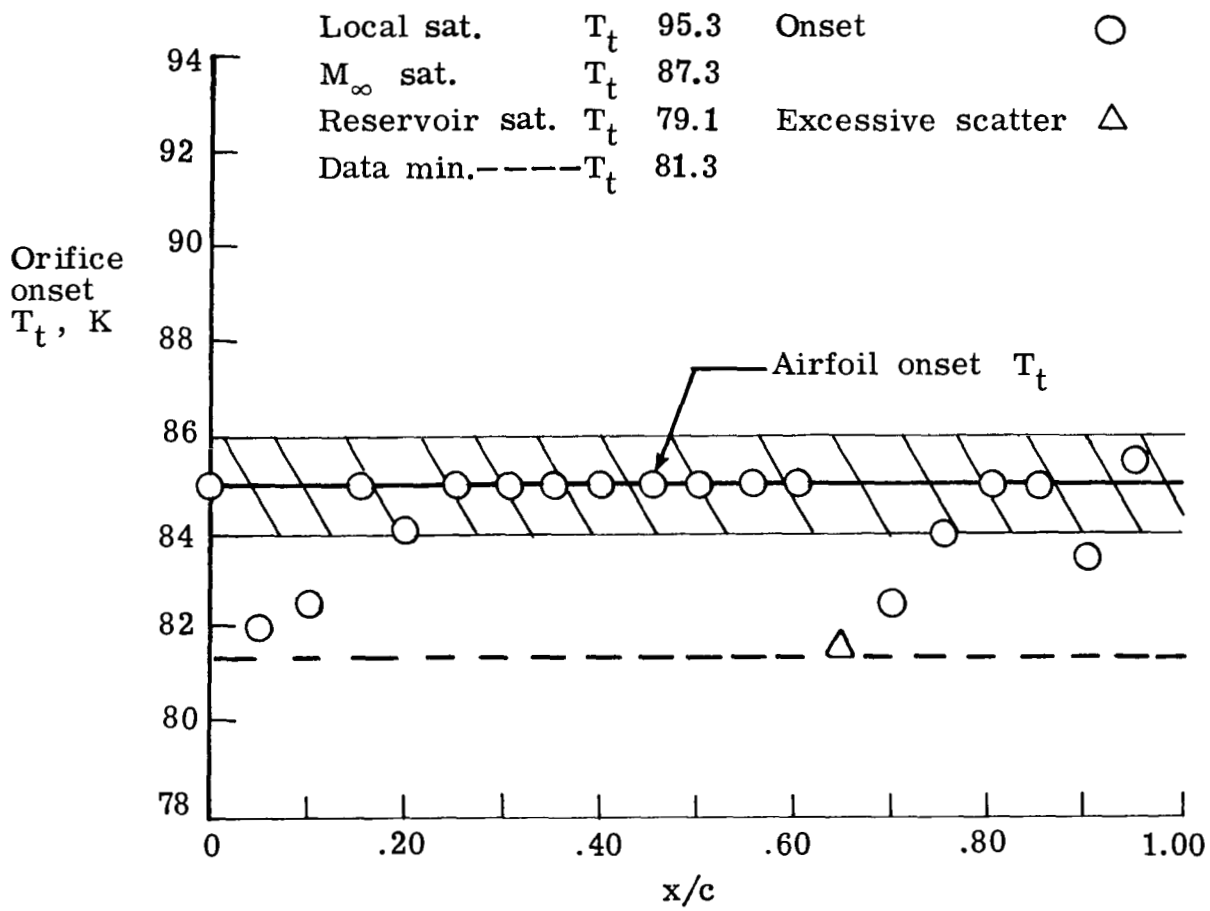

Figure 19.- Orifice onset T_t's and resulting airfoil onset T_t for $R_c = 16 \times 10^6$ path of $M_\infty = 0.85$ test.

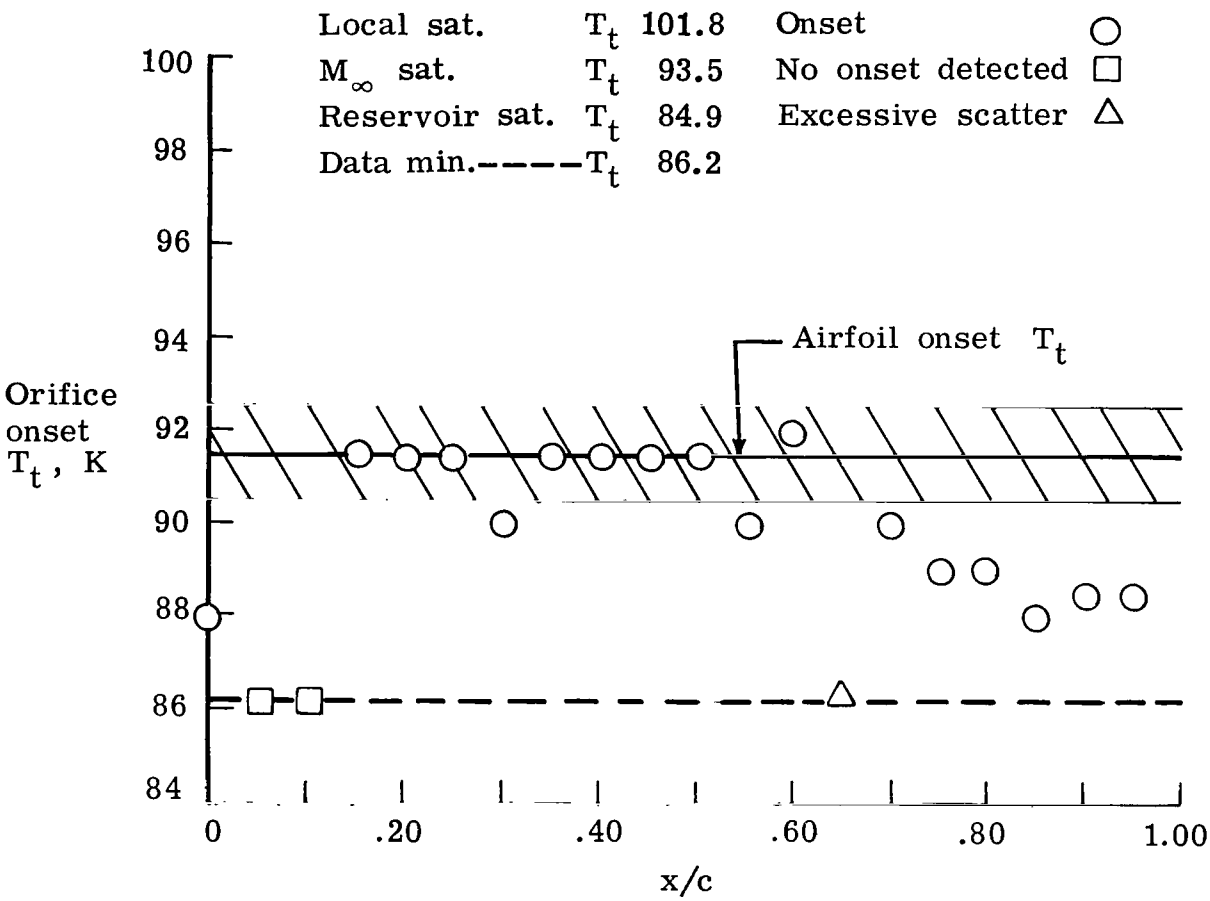

Figure 20.- Orifice onset T_t's and resulting airfoil onset T_t for $R_c = 26 \times 10^6$ of $M_\infty = 0.85$ test.

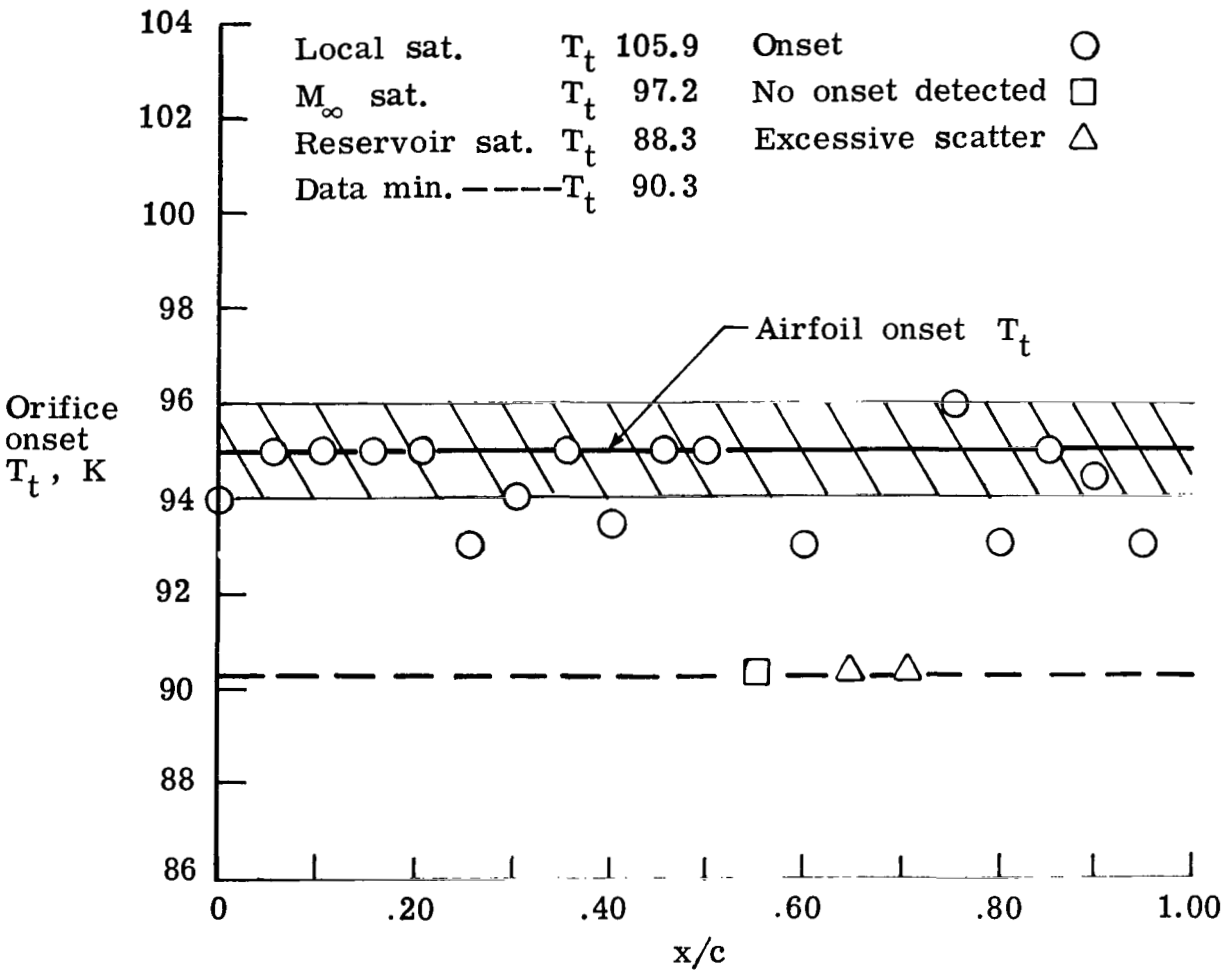

Figure 21.- Orifice onset T_t's and resulting airfoil onset T_t for $R_c = 34 \times 10^6$ path of $M_\infty = 0.85$ test.

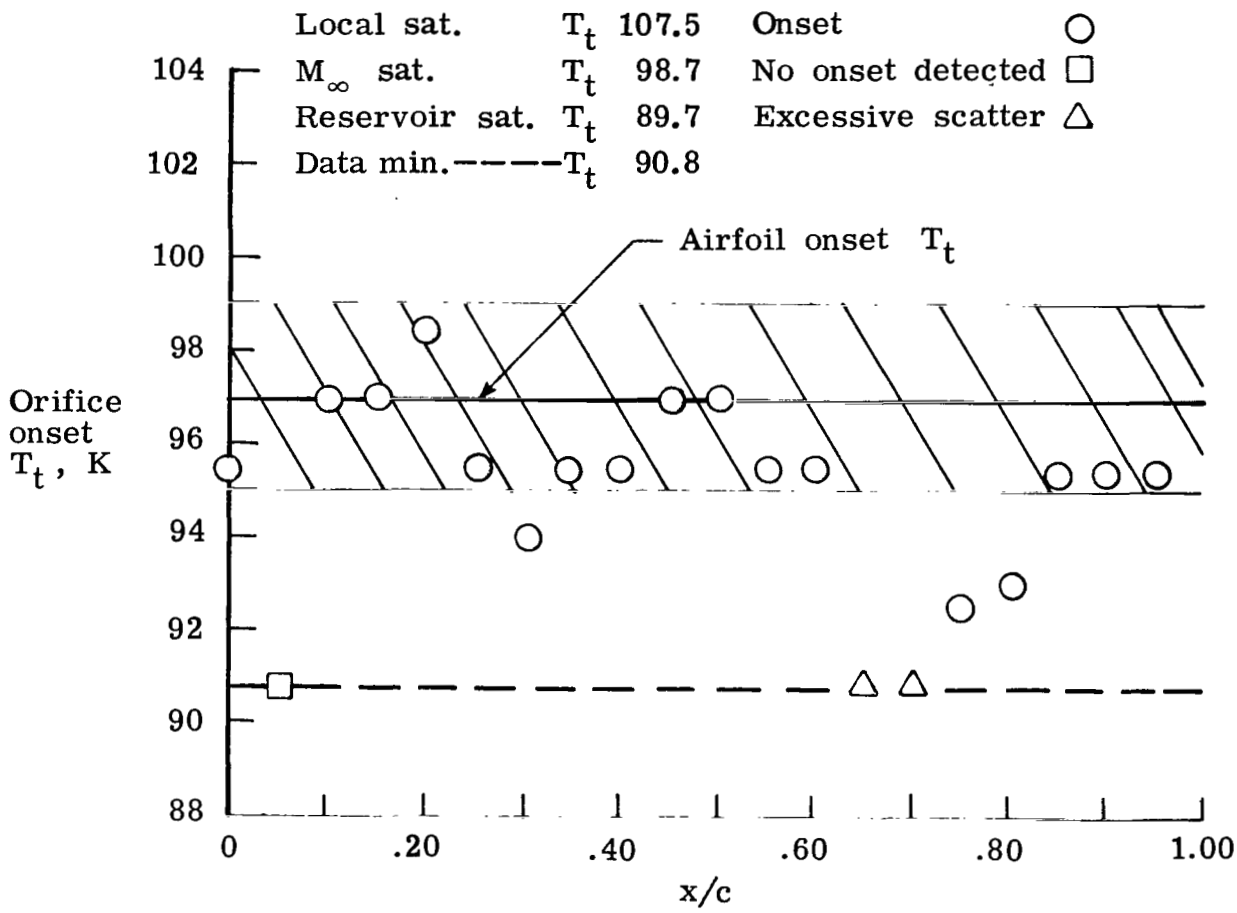

Figure 22.- Orifice onset T_t's and resulting airfoil onset T_t for $R_c = 38 \times 10^6$ path of $M_\infty = 0.85$ test.

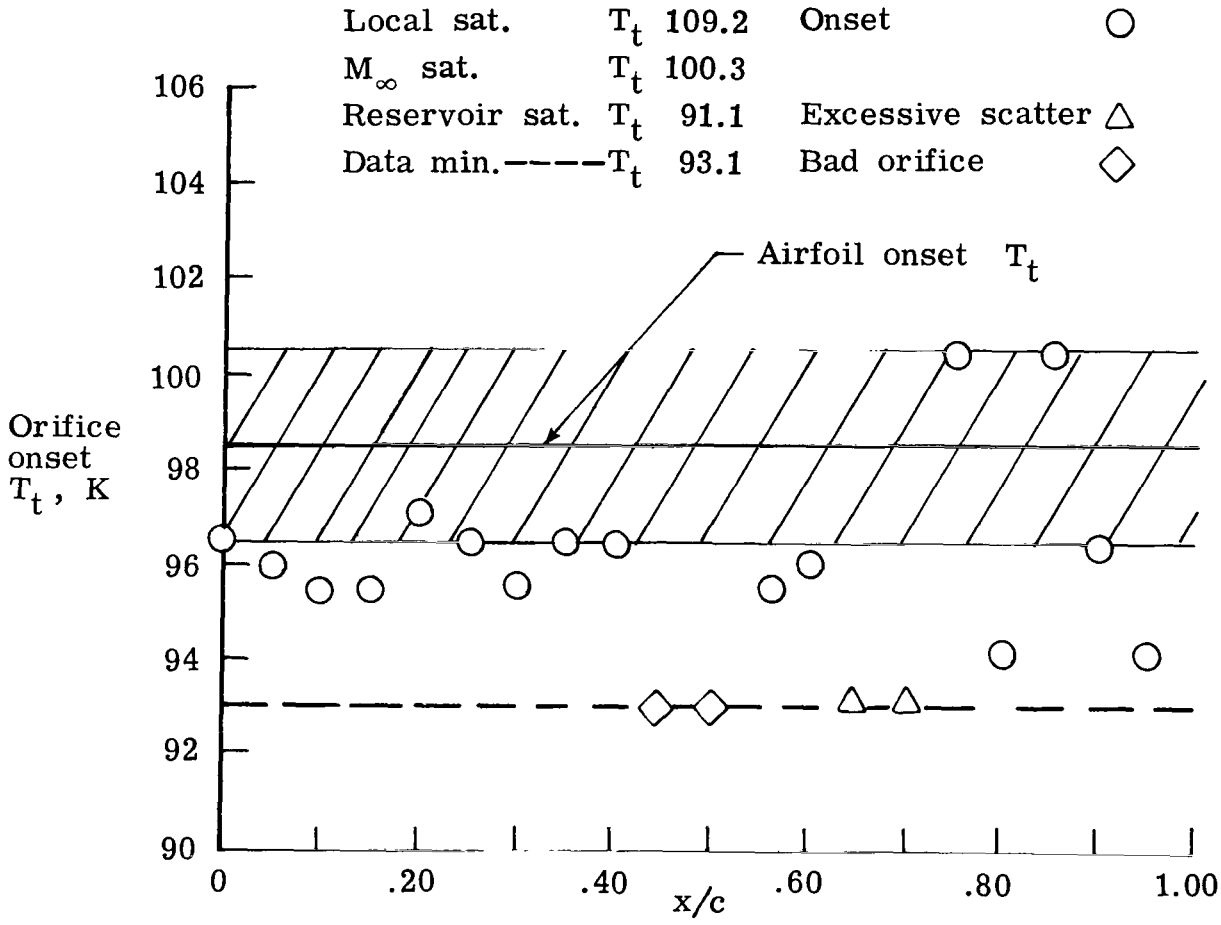

Figure 23.- Orifice onset T_t's and resulting airfoil onset T_t for $R_c = 42 \times 10^6$ path of $M_\infty = 0.85$ test.

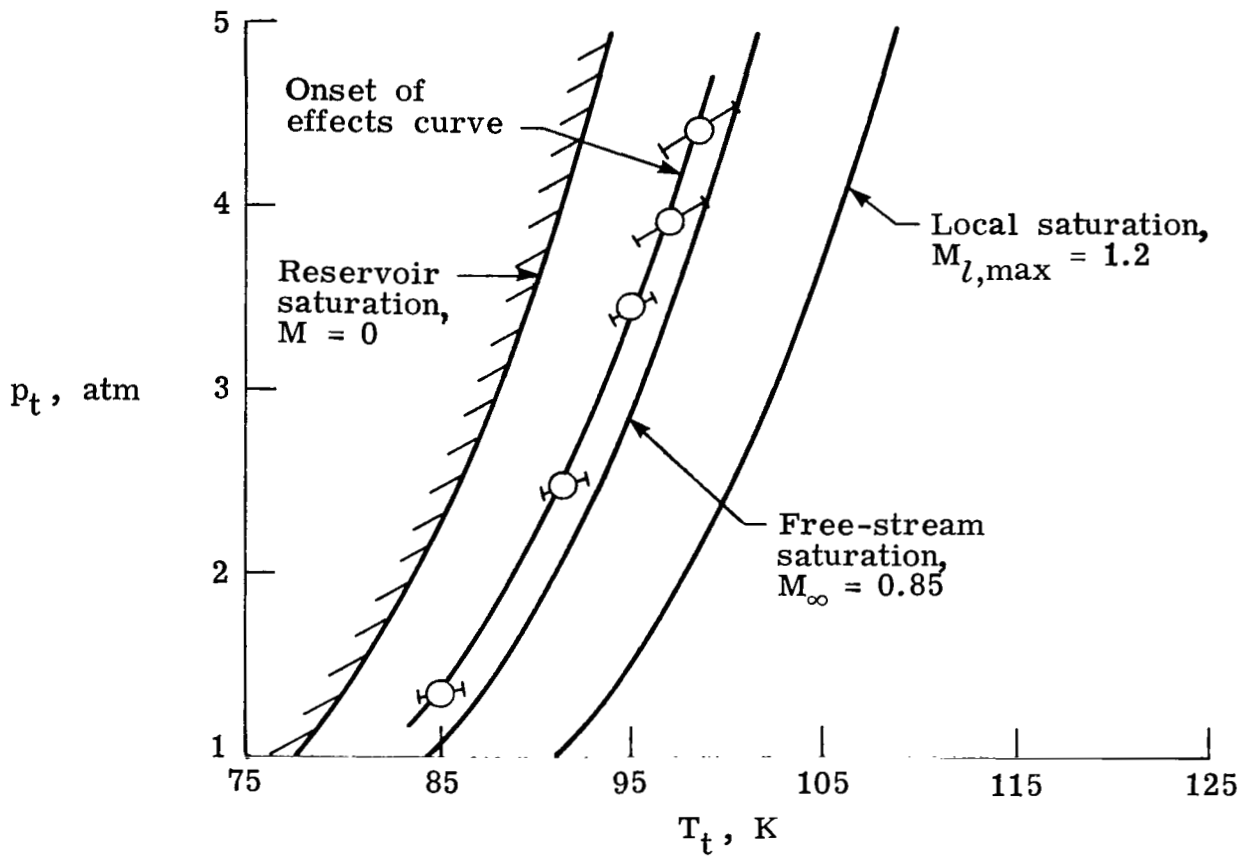

Figure 24.- Onset of condensation effects for M_∞ = 0.85 test.
Error bars shown indicate possible experimental error.

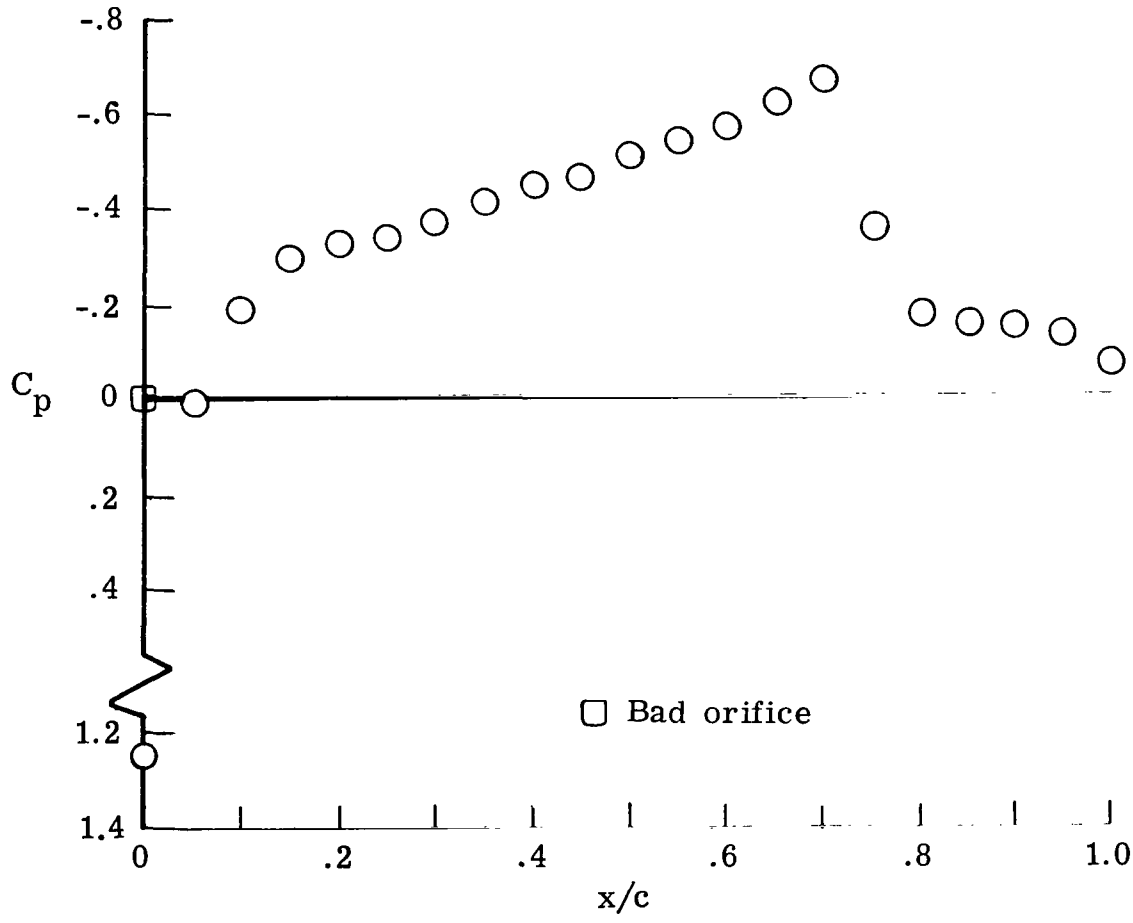

Figure 25.- Average unaffected pressure distribution for $R_C = 17 \times 10^6$ path of $M_\infty = 0.95$ test.

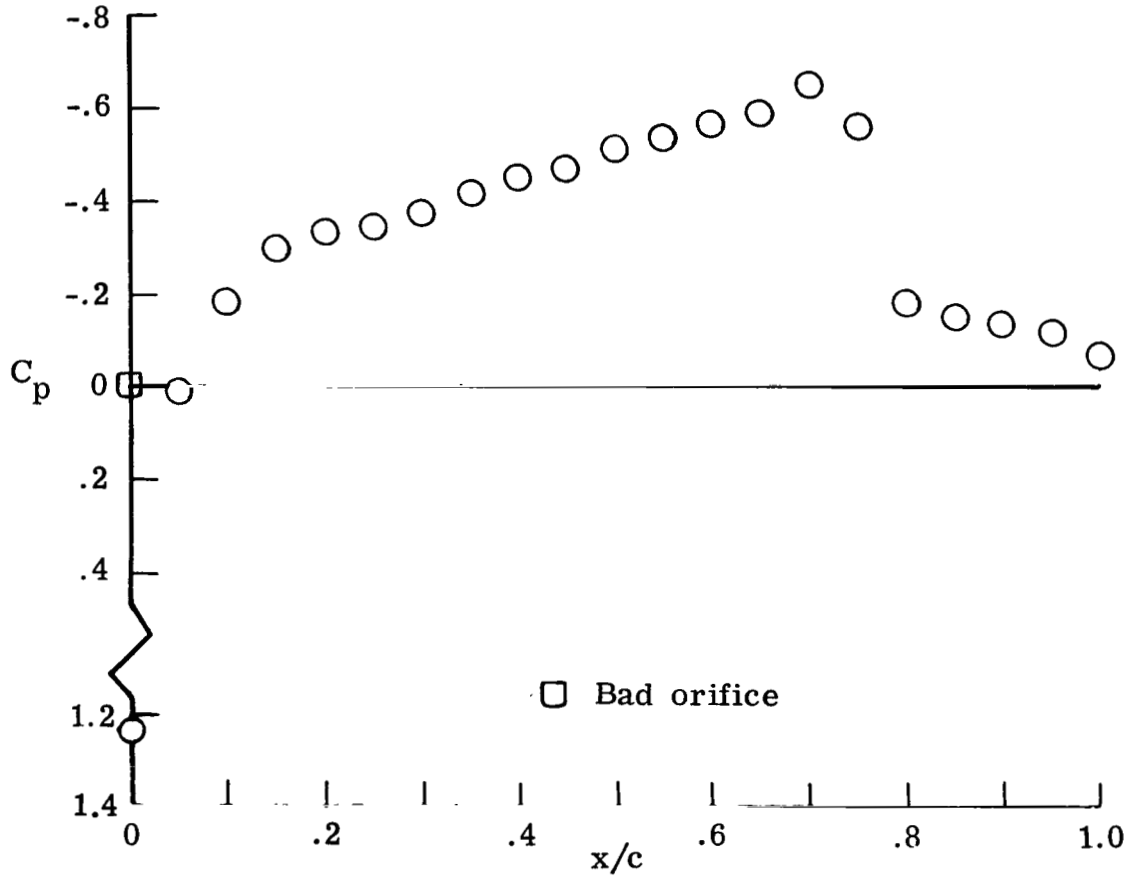

Figure 26.- Average unaffected pressure distribution for $R_c = 27 \times 10^6$ path of $M_\infty = 0.95$ test.

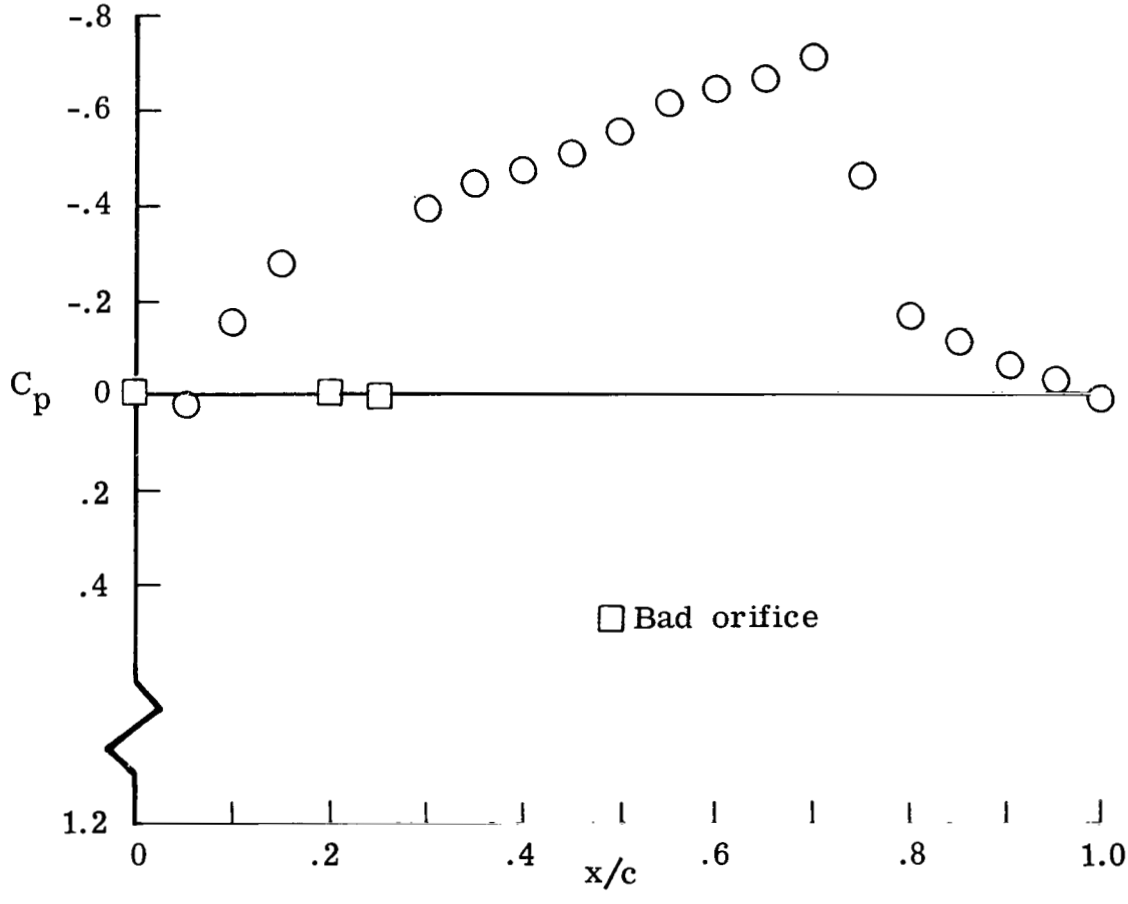

Figure 27.- Average unaffected pressure distribution for $R_c = 40 \times 10^6$ path of $M_\infty = 0.95$ test. ($M_\infty = 0.93$ for this path.)

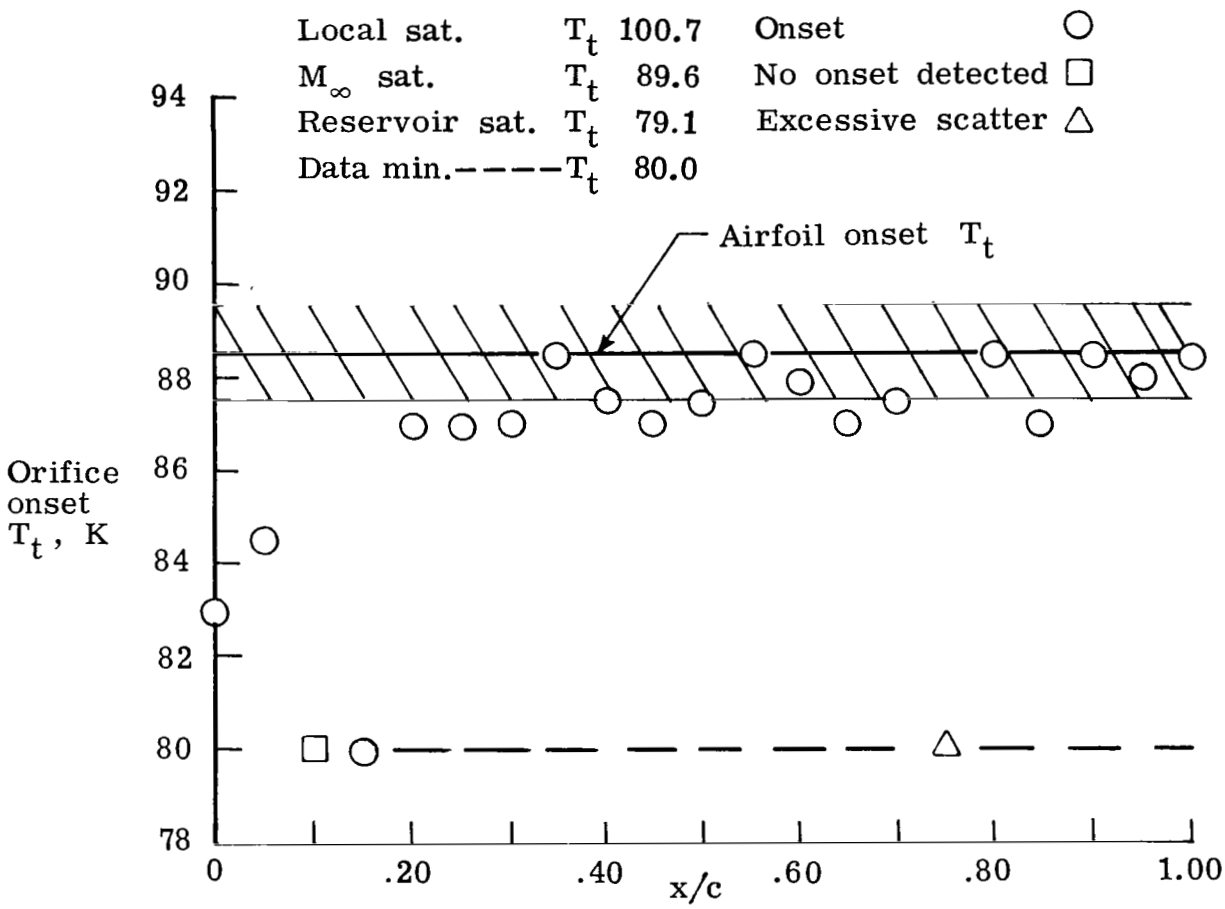

Figure 28.- Orifice onset T_t's and resulting airfoil onset T_t for $R_c = 17 \times 10^6$ path of $M_\infty = 0.95$ test.

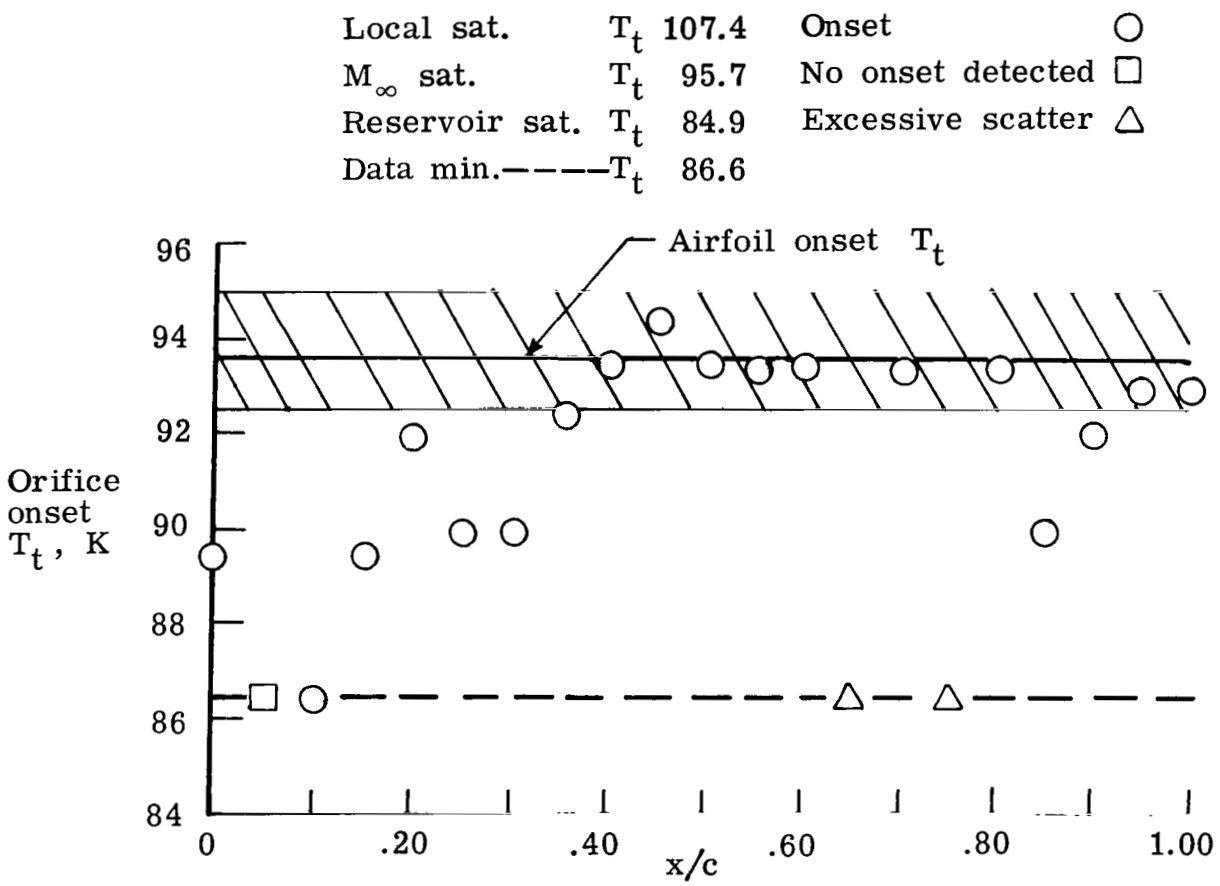

Figure 29.- Orifice onset T_t's and resulting airfoil onset T_t for $R_c = 27 \times 10^6$ path of $M_\infty = 0.95$ test.

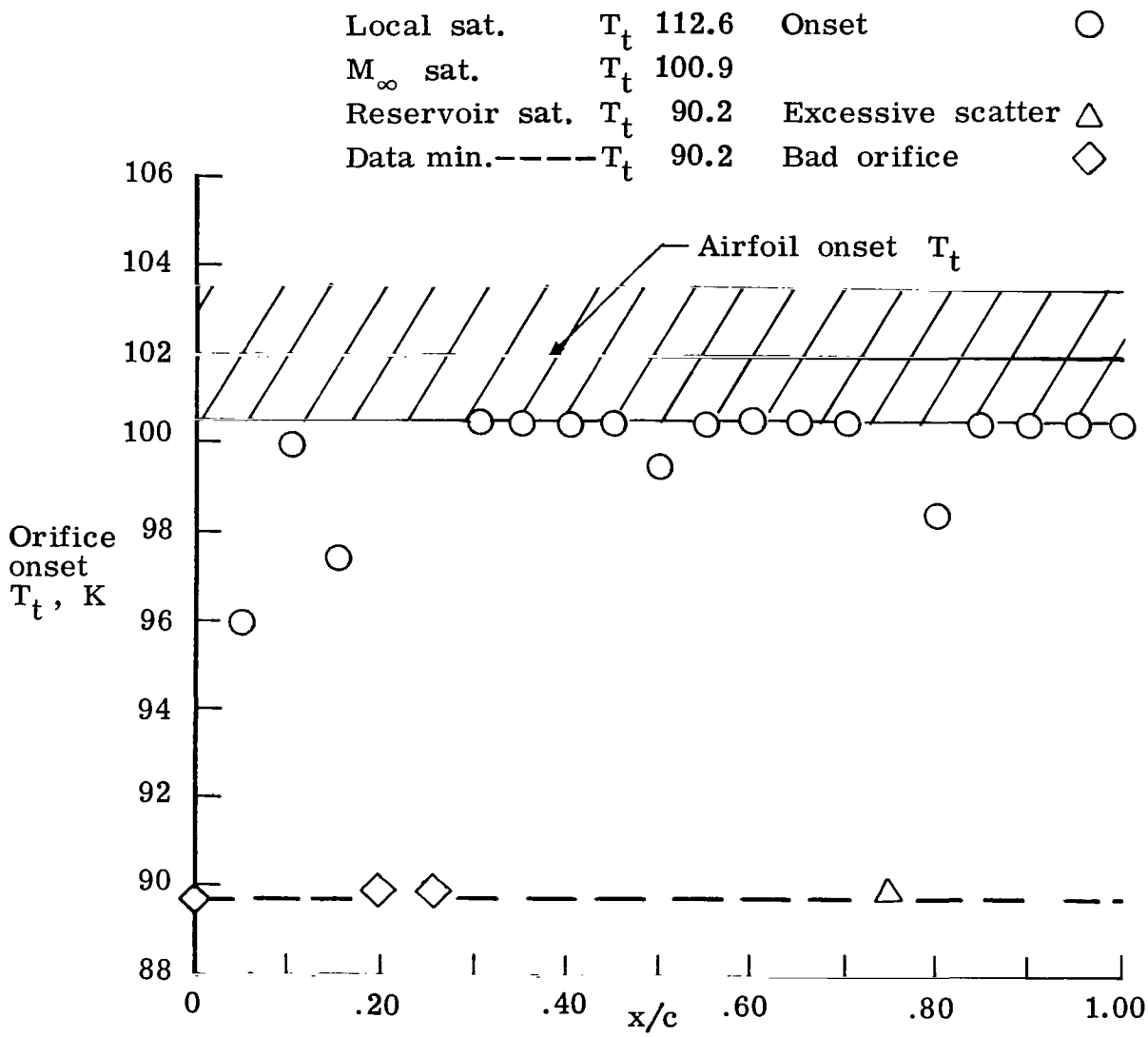

Figure 30.- Orifice onset T_t's and resulting airfoil onset T_t for $R_c = 40 \times 10^6$ path with $M_\infty = 0.93$.

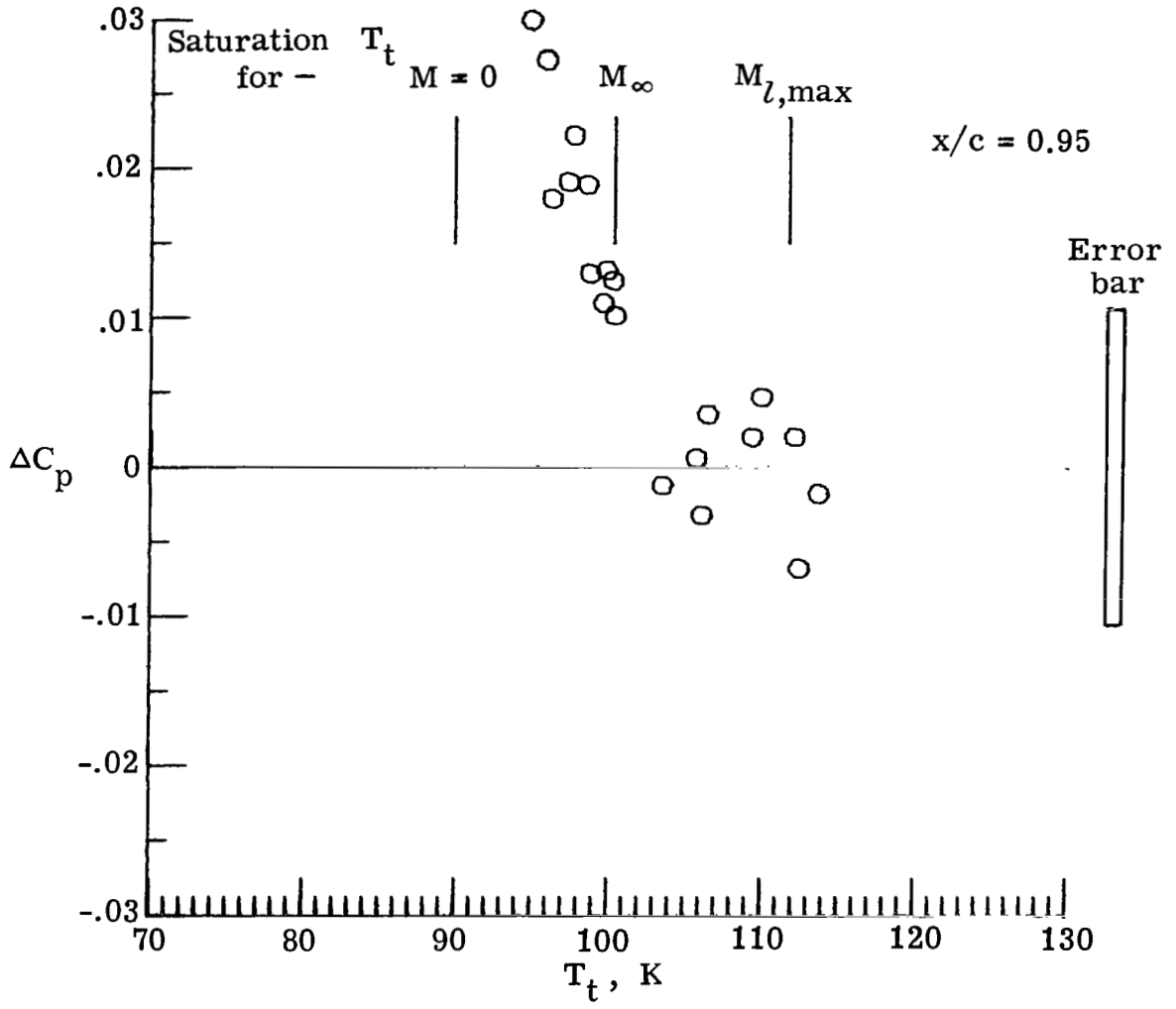

Figure 31.- ΔC_p plotted against T_t for $M_\infty = 0.93$ and $R_c = 40 \times 10^6$. Unaffected average value of $C_p = -0.035$.

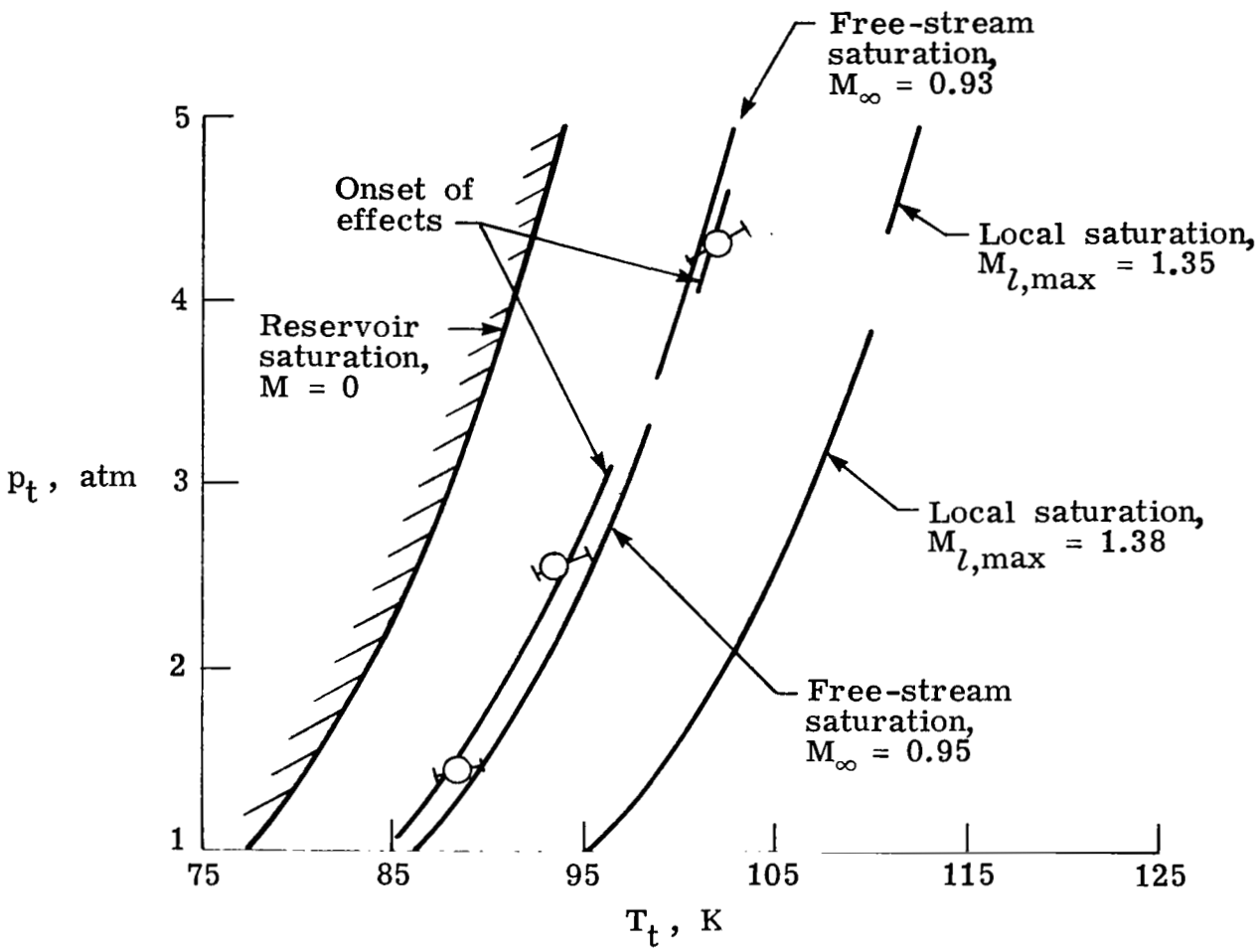

Figure 32.- Onset of condensation effects for M_∞ = 0.95 test.
Error bars shown indicate possible experimental error.

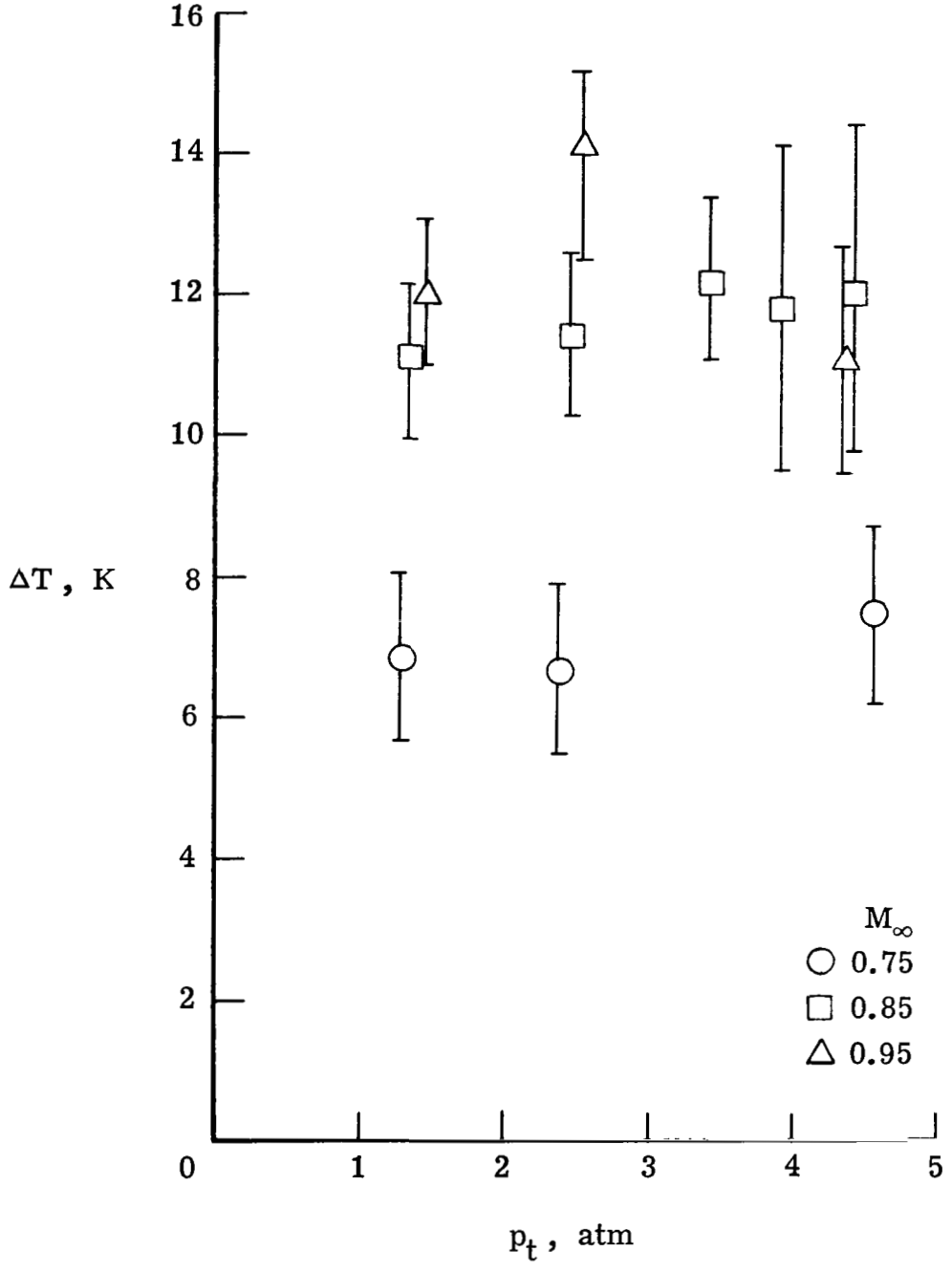

(a) Supercooling based on $M_{l,max}$.

Figure 33.- Supercooling for all M_∞ tests. Error bars shown indicate possible experimental error.

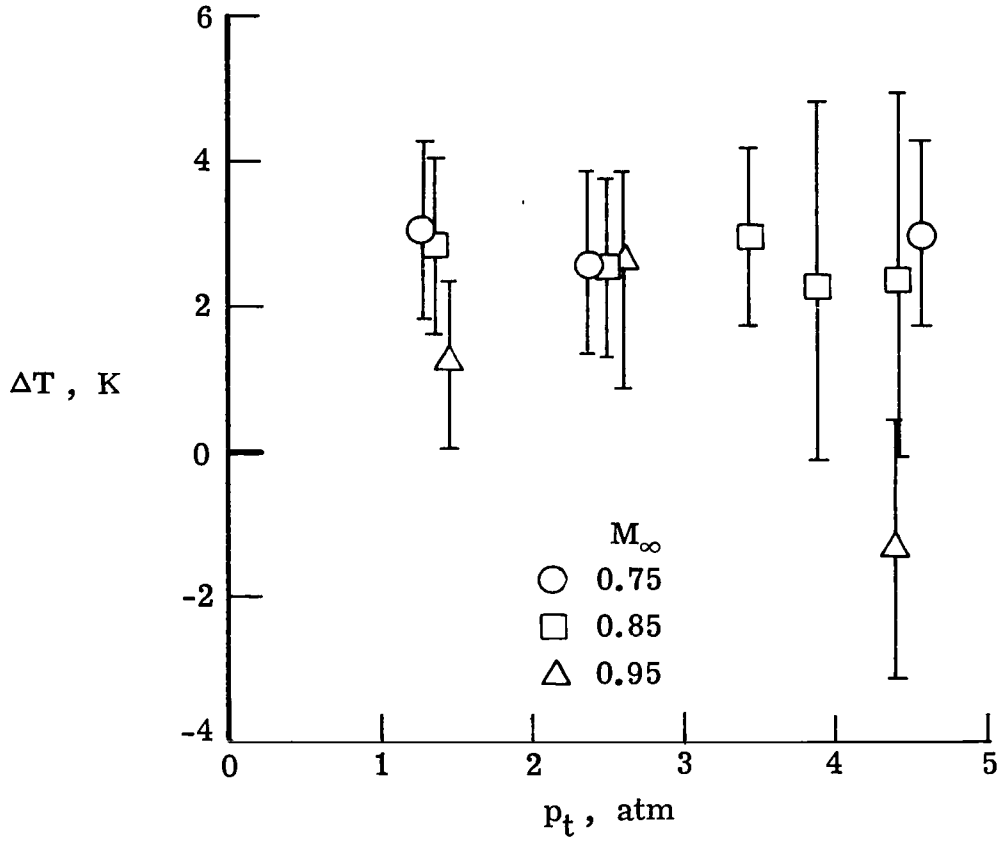

(b) Supercooling based on M_∞.

Figure 33.- Concluded.

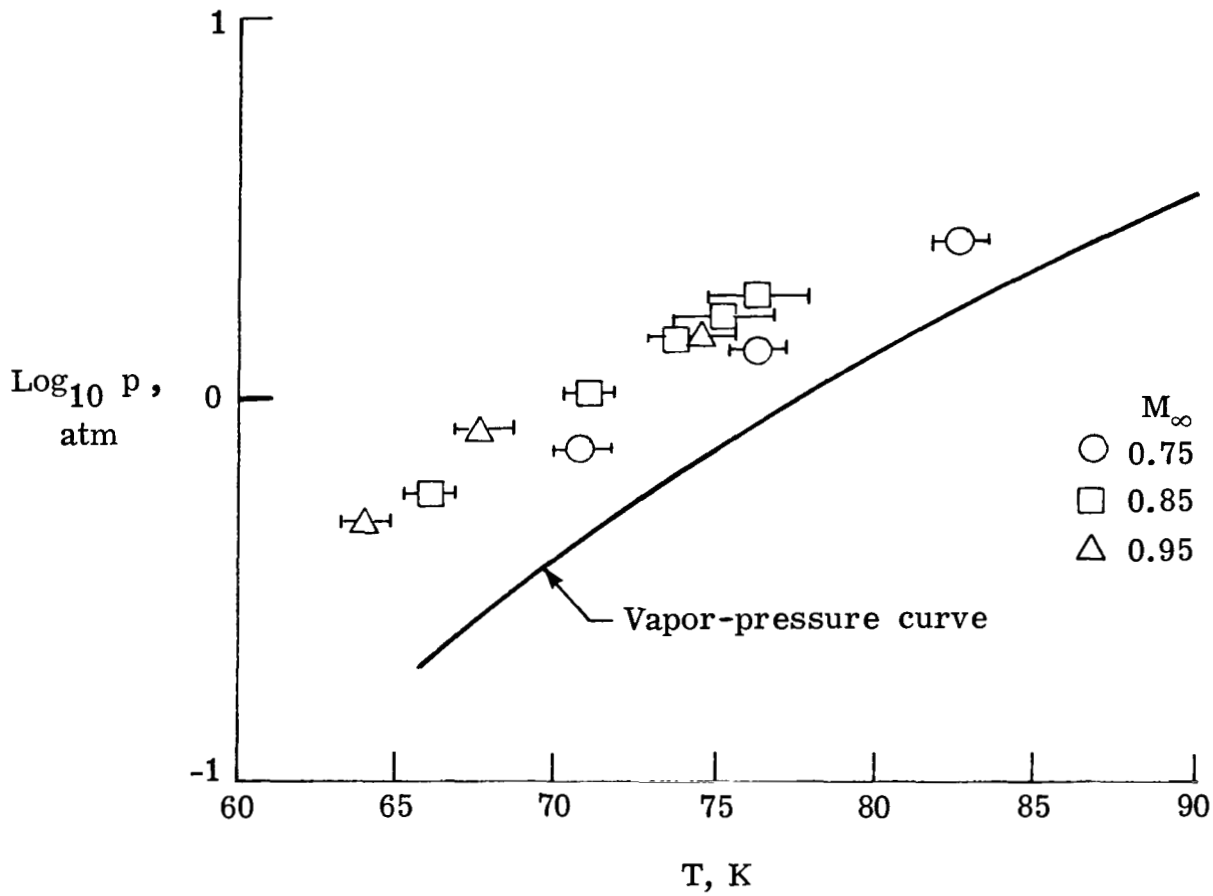

(a) Static values based on $M = M_{l,max}$.

Figure 34.- Static values of p, T at onset. Error bars shown indicate possible experimental error.

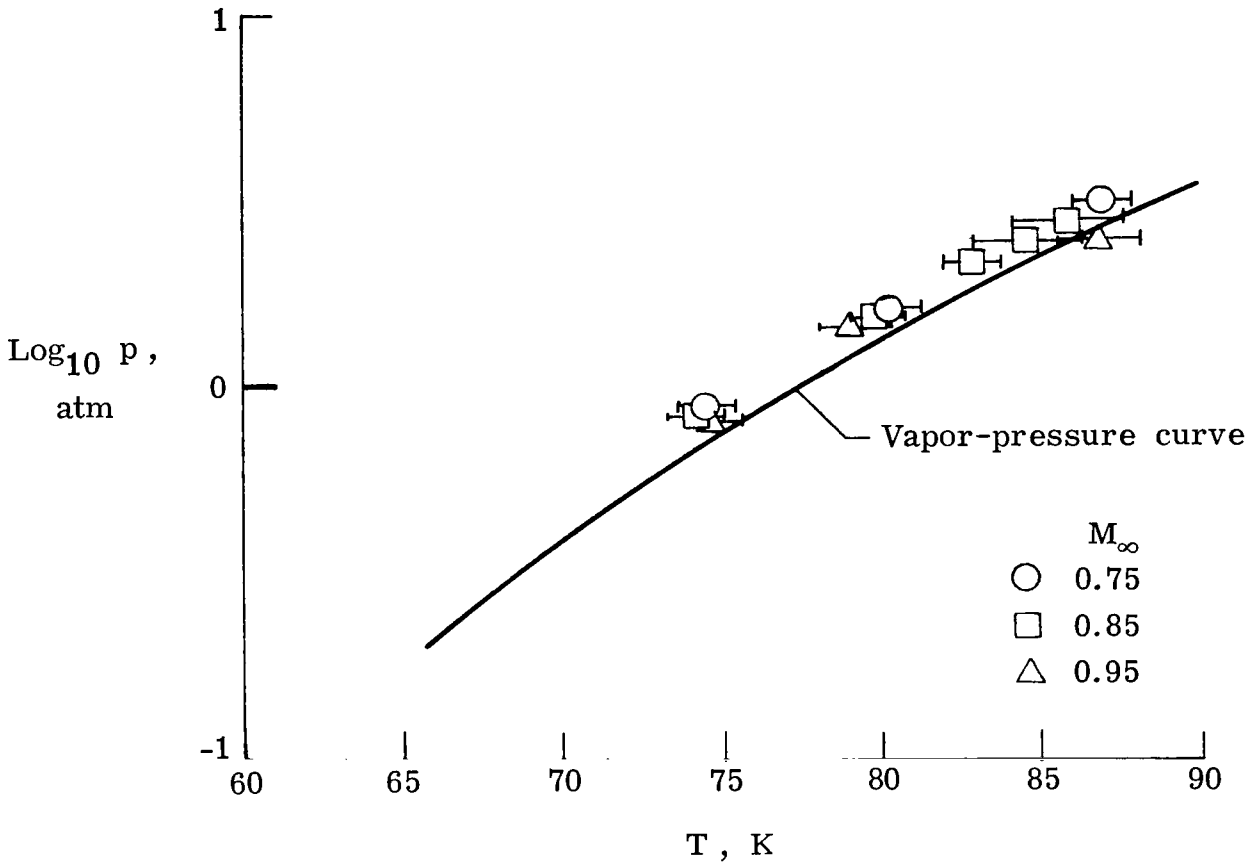

(b) Static values based on $M = M_\infty$.

Figure 34.- Concluded.

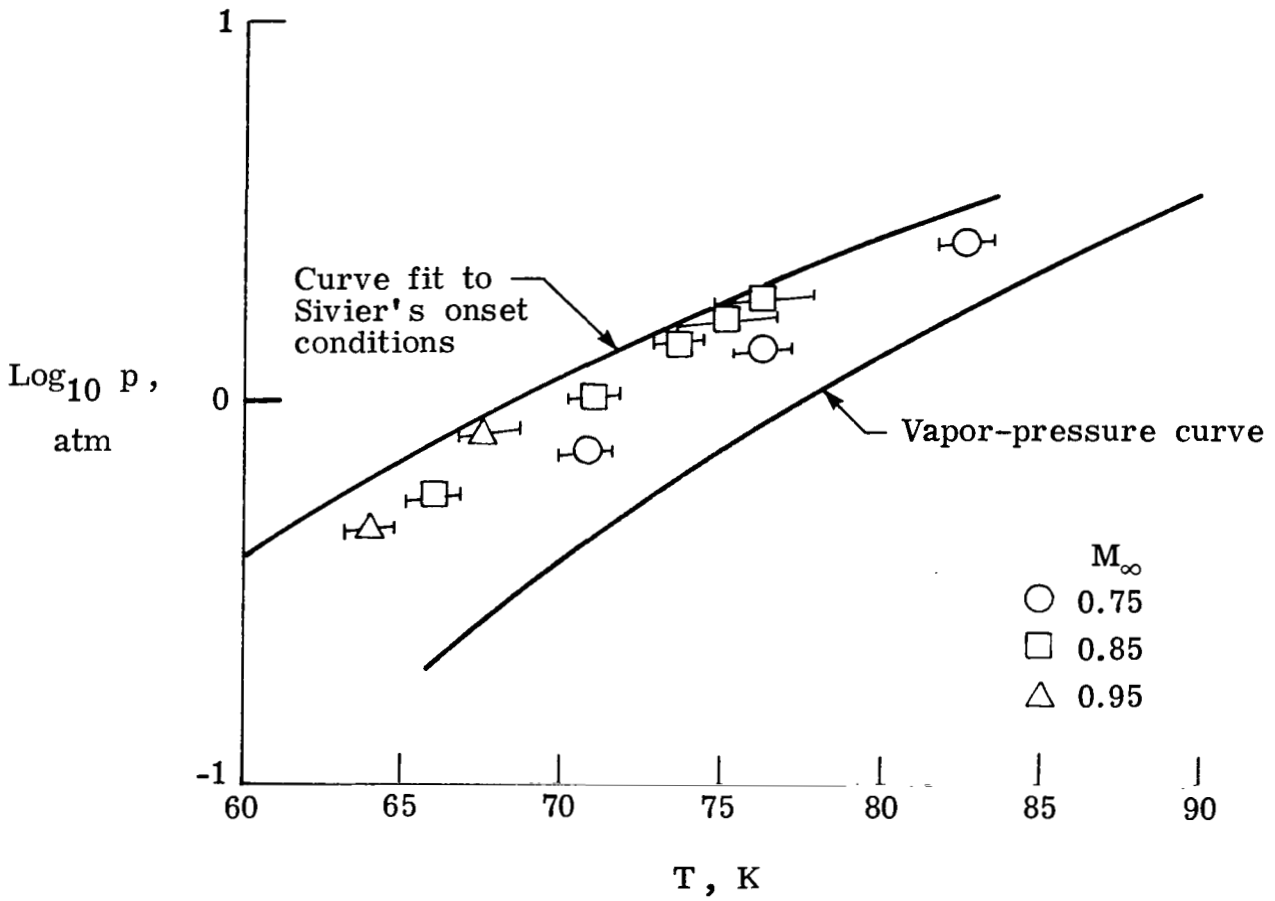

Figure 35.- Data compared with Adcock's curve fit to Sivier's analytically determined onset conditions. Error bars indicate possible experimental error.

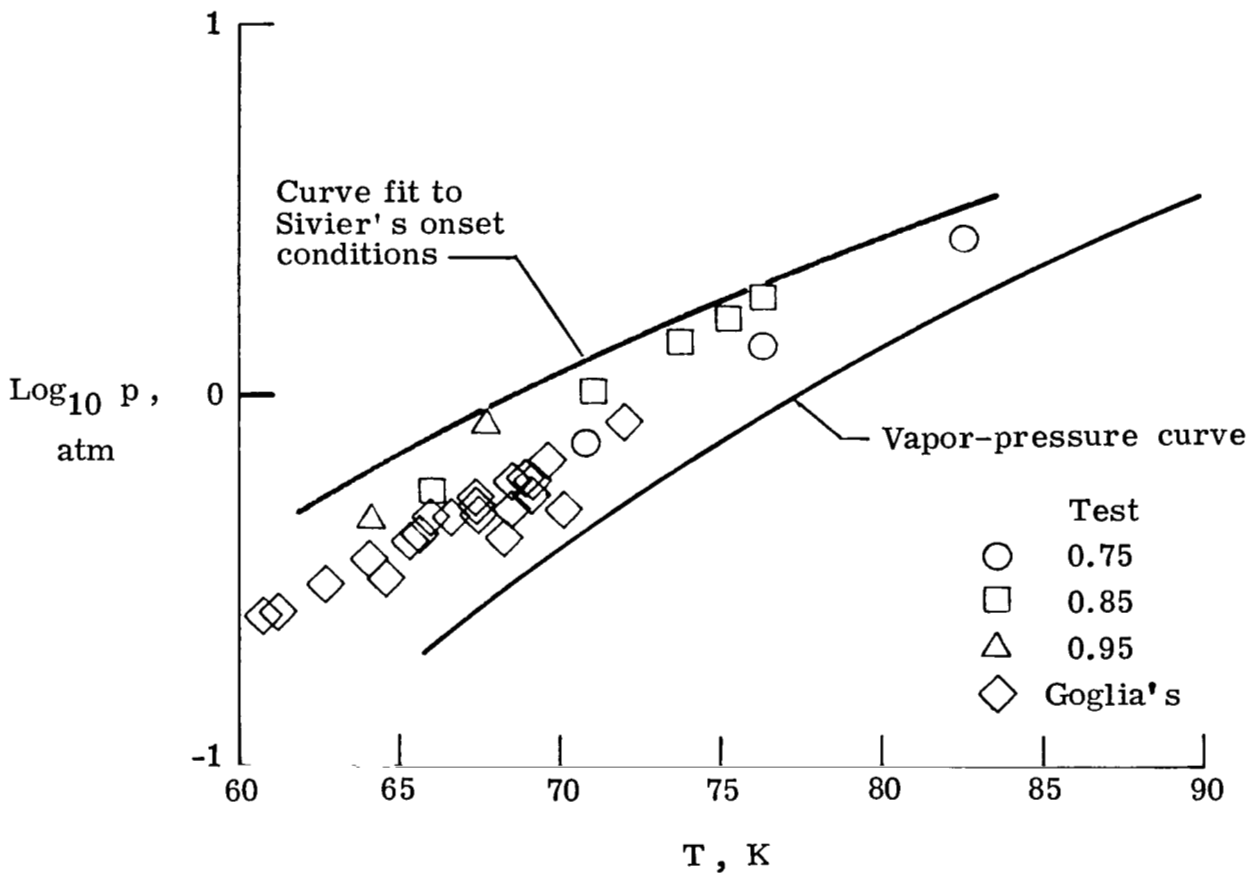

Figure 36.- Present data compared with Goglia's data from reference 17.

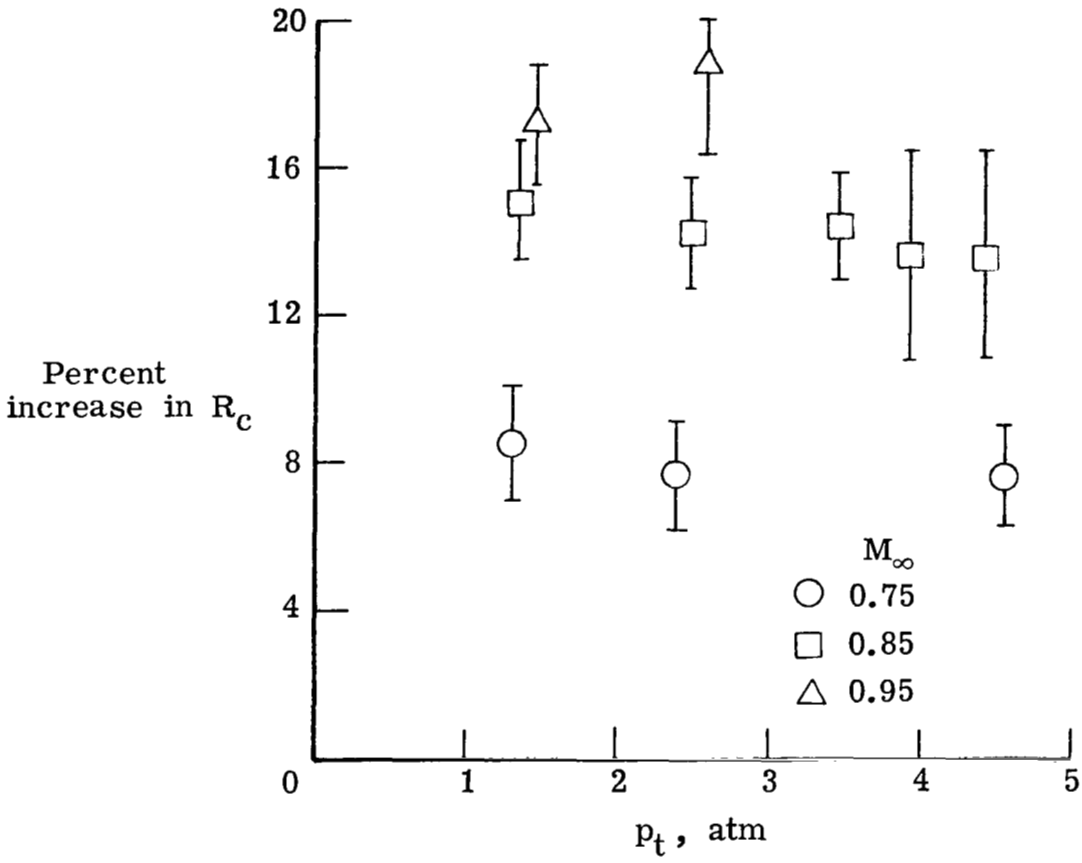

Figure 37.- Percent increase in Reynolds number capability at onset. Error bars shown indicate possible experimental error.

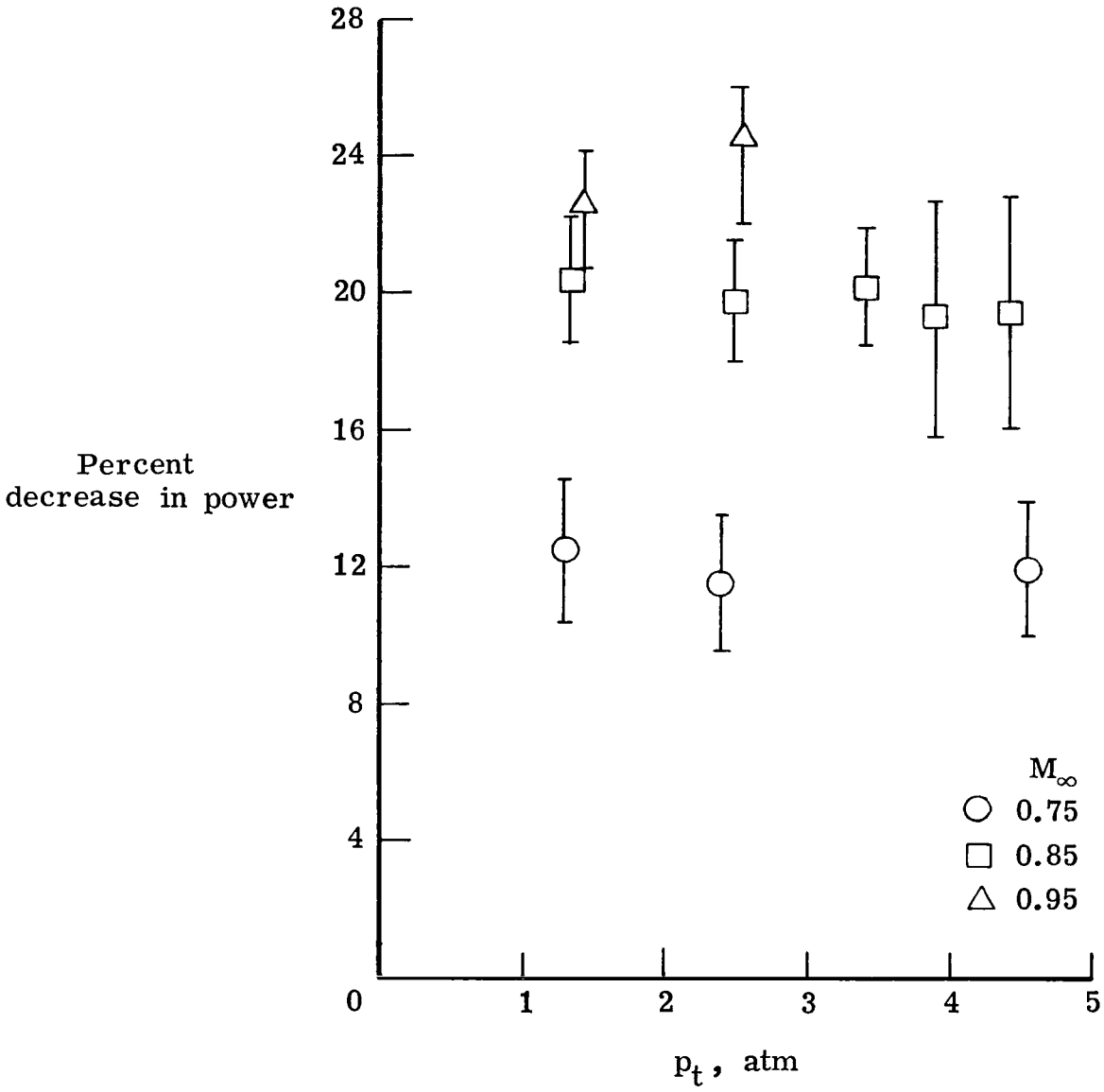

Figure 38.- Percent decrease in drive-fan power at onset. Error bars shown indicate possible experimental error.

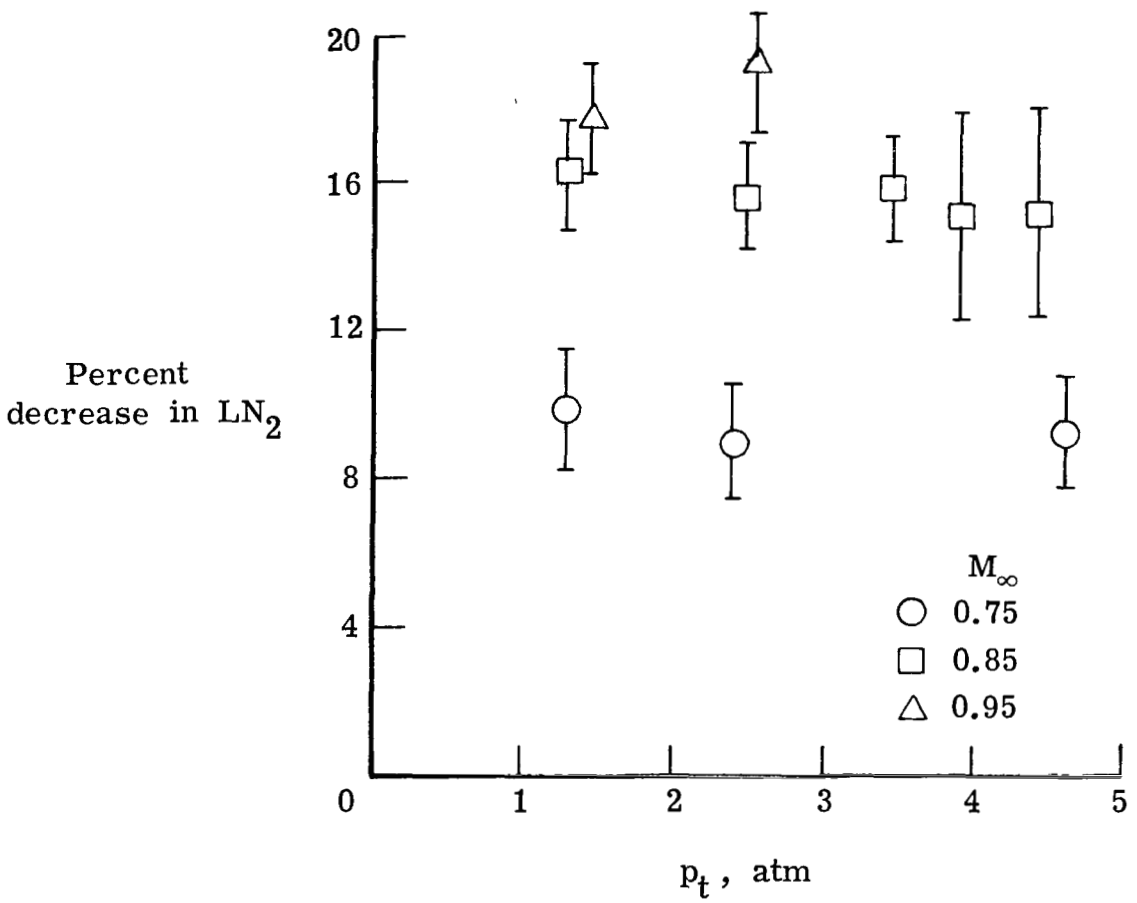

Figure 39.- Percent decrease in LN_2 required to absorb drive-fan heat. Error bars shown indicate possible experimental error.

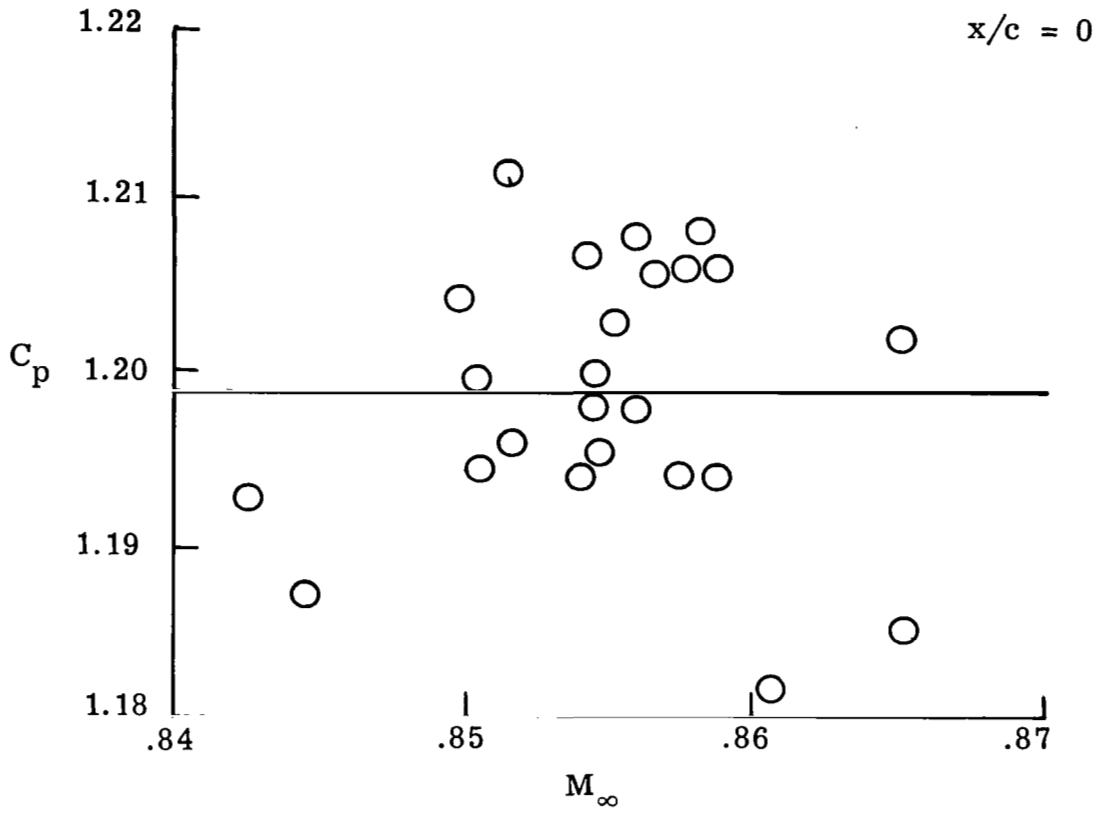

(a) r = 0.15.

Figure 40.- Examples of curve fits and resulting correlation coefficient r.

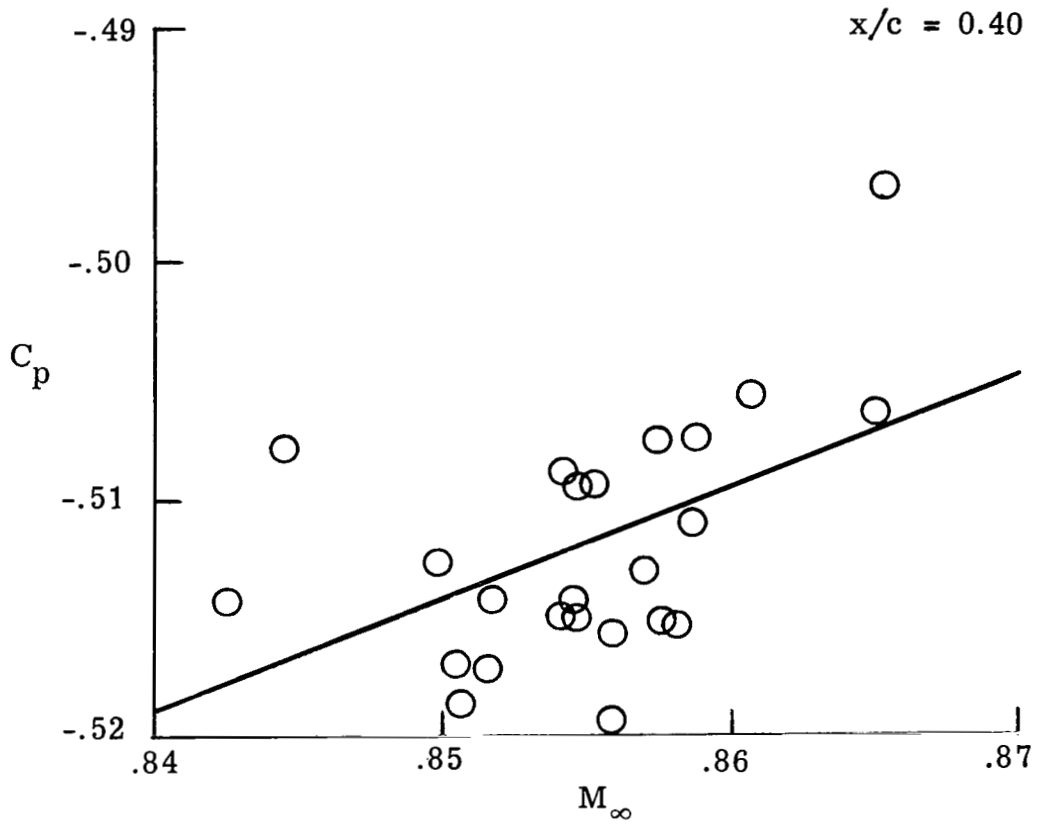

(b) r = 0.49.

Figure 40.- Continued.

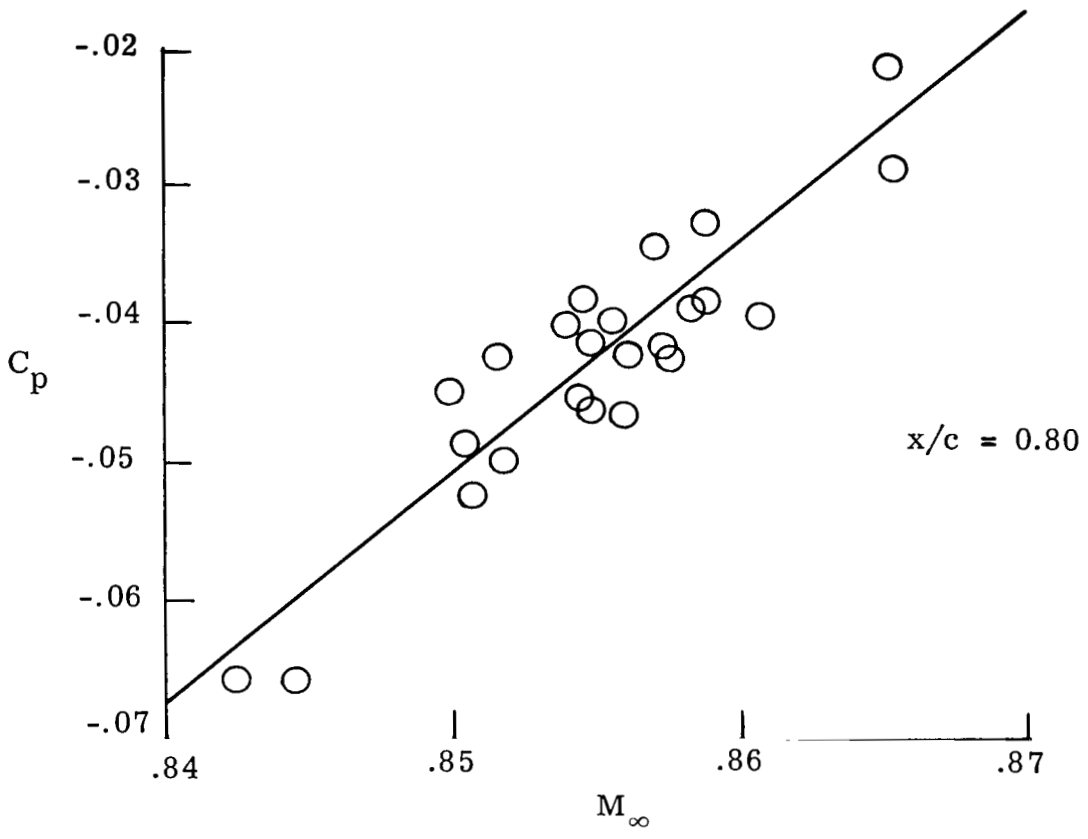

(c) r = 0.92.

Figure 40.- Concluded.

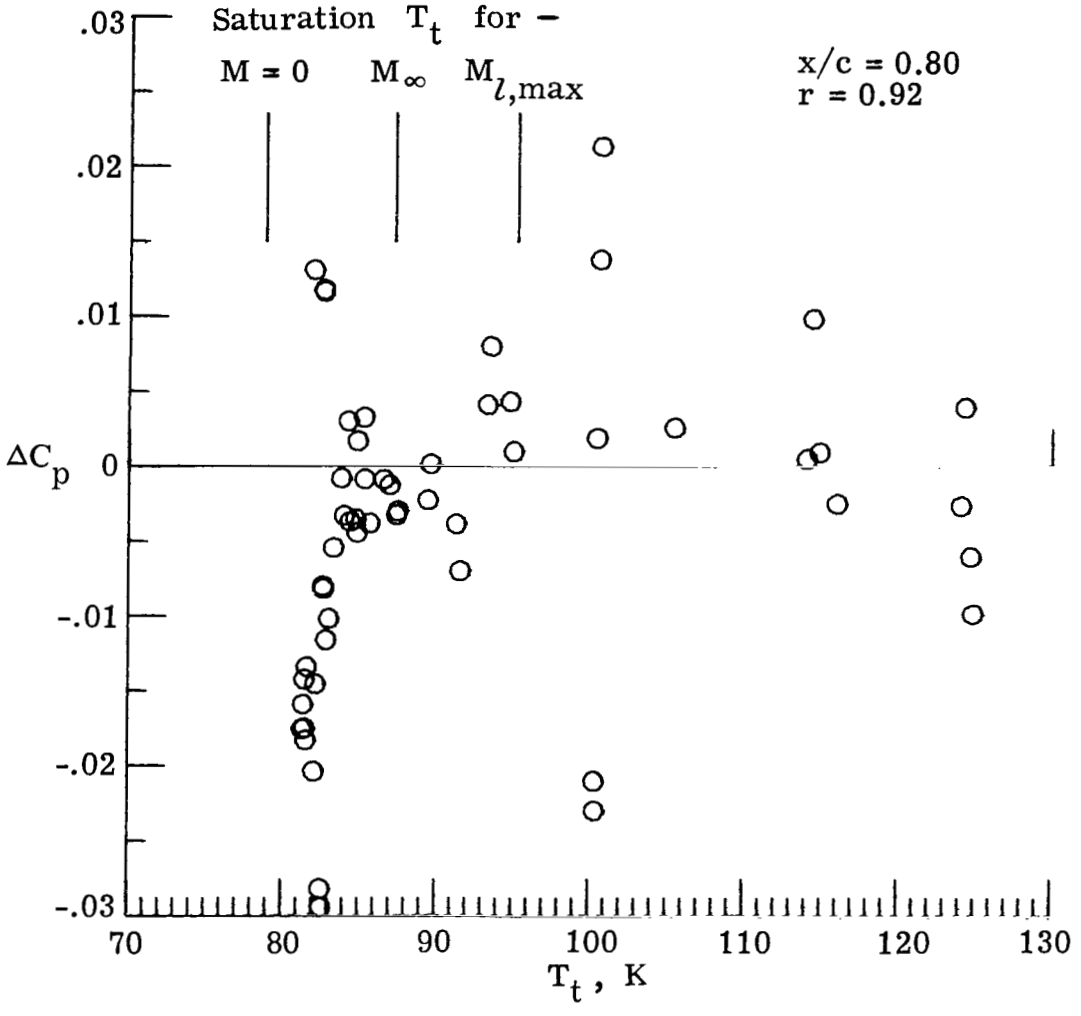

(a) Before M_∞ correction procedure.

Figure 41.- Improvement in graphs of ΔC_p plotted against T_t with Mach correction for $M_\infty = 0.85$ and $R_c = 16 \times 10^6$. Unaffected average value of $C_p = -0.042$.

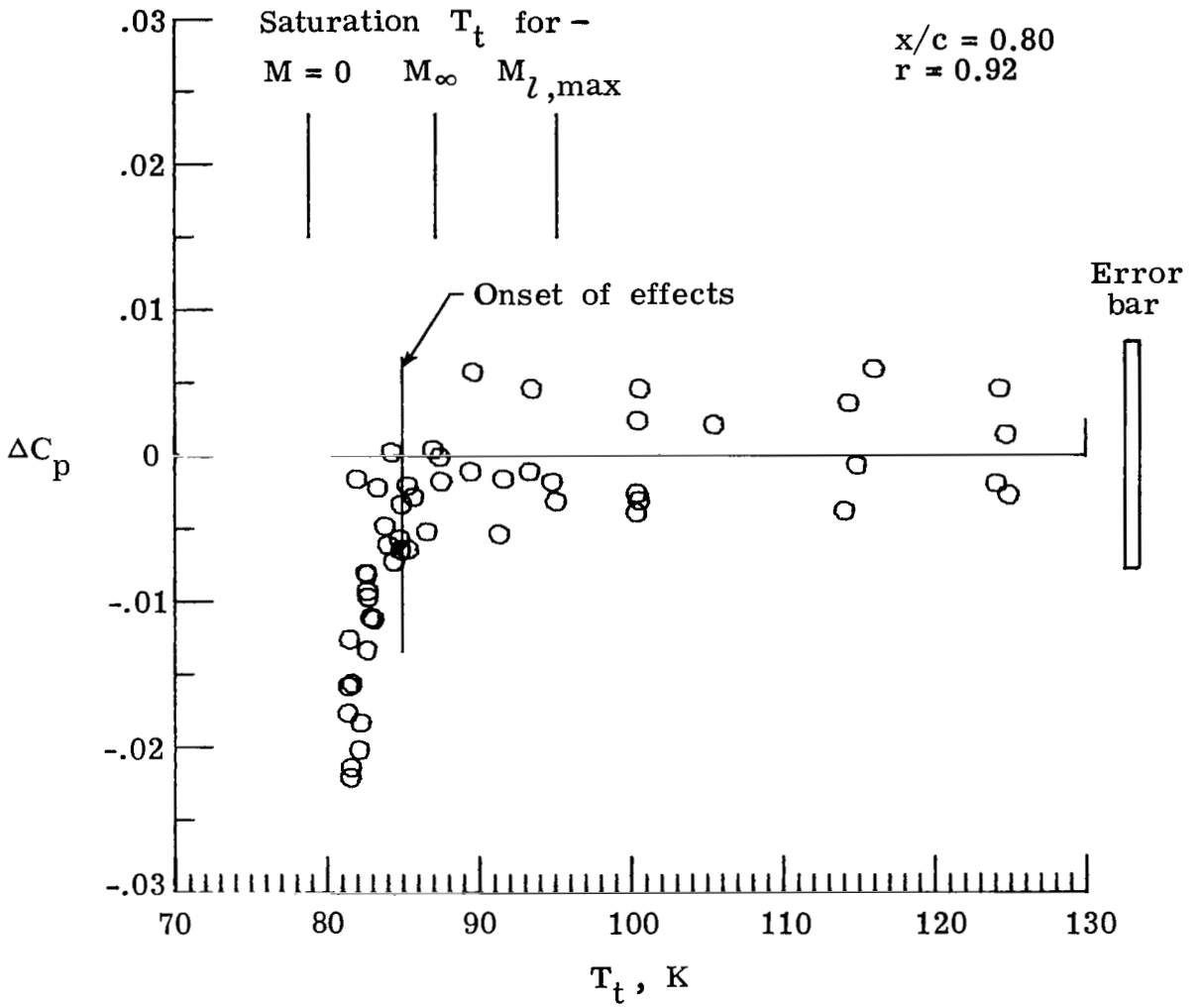

(b) After M_∞ correction procedure.

Figure 41.- Concluded.

1. Report No.	2. Government Accession No.	3. Recipient's Catalog No.
NASA TP-1385		

4. Title and Subtitle	5. Report Date
ONSET OF CONDENSATION EFFECTS WITH AN NACA 0012-64 AIRFOIL TESTED IN THE LANGLEY 0.3-METER TRANSONIC CRYOGENIC TUNNEL	April 1979
	6. Performing Organization Code
7. Author(s)	8. Performing Organization Report No.
Robert M. Hall	L-12581
	10. Work Unit No.
9. Performing Organization Name and Address	505-06-43-08
NASA Langley Research Center Hampton, VA 23665	11. Contract or Grant No.
	13. Type of Report and Period Covered
12. Sponsoring Agency Name and Address	Technical Paper
National Aeronautics and Space Administration Washington, DC 20546	14. Sponsoring Agency Code

15. Supplementary Notes

16. Abstract

A 0.137-meter NACA 0012-64 airfoil has been tested at a 0° angle of attack in the nitrogen-gas Langley 0.3-meter transonic cryogenic tunnel at free-stream Mach numbers of 0.75, 0.85, and 0.95 over a total pressure range from 1.2 to 5.0 atmospheres. The onset of condensation effects as determined by varying the stagnation temperature was found to correlate better with the amount of supercooling in the free stream than it did with the supercooling in the region of maximum local Mach number over the airfoil. Effects in the pressure distribution over the airfoil were generally seen to appear over its entire length at nearly the same total temperature. Both observations suggest that heterogeneous nucleation does occur in the free stream. The benefits realized from supercooling are presented in terms of increased Reynolds number capability at a given tunnel total pressure and reduced drive-fan power and liquid nitrogen consumption if Reynolds number is held constant. Depending on total pressure and free-stream Mach number, these three benefits are found to vary respectively from 8 to 19 percent, 12 to 24 percent, and 9 to 19 percent. The appendix gives details of the data analysis and error estimates.

17. Key Words (Suggested by Author(s))	18. Distribution Statement
Cryogenic wind tunnels Condensation Minimum temperatures	Unclassified - Unlimited Subject Category 02

19. Security Classif. (of this report)	20. Security Classif. (of this page)	21. No. of Pages	22. Price*
Unclassified	Unclassified	69	$5.25

* For sale by the National Technical Information Service, Springfield, Virginia 22161

NASA-Langley, 1979

2 1 1U,A, 042079 S00903DS
DEPT OF THE AIR FORCE
AF WEAPONS LABORATORY
ATTN: TECHNICAL LIBRARY (SUL)
KIRTLAND AFB NM 87117